*The Canadian Mineralogist*
Vol. 52, pp. 191-219 (2014)
DOI: 10.3749/canmin.52.2.191

# TERTIARY PEGMATITE DIKES OF THE CENTRAL ALPS

A. GUASTONI§

*Museum of Mineralogy, University of Padova, Via Matteotti 30, I-35121, Padova, Italy*

G. PENNACCHIONI AND G. POZZI

*Department of Geosciences, University of Padova, Via Gradenigo 6, I-35131 Padova, Italy*

A.M. FIORETTI

*CNR – Istituto di Geoscienze e Georisorse, Via Gradenigo 6, I-35131 Padova, Italy*

J.M. WALTER

*Geowissenschaftliches Zentrum, Universität Göttingen (GZG), Goldschmidtstraße 1-3, D-37077, Göttingen, Germany*

## ABSTRACT

The largest field of Alpine Oligocene pegmatite dikes is in the Central Alps within the Southern Steep Belt (SSB) of the Alpine nappes; it extends for about 100 km in an E–W direction and 15 km in a N–S direction north of the Periadriatic Fault, from the Bergell pluton (to the east) to the Ossola valley (to the west). The pegmatite field geographically overlaps (1) the highest temperature domain of the Lepontine Barrovian metamorphic dome and (2) the zone of Alpine migmatization. We have studied pegmatites in two areas: (1) the Codera area on the western border of the Bergell pluton and (2) the Bodengo area between the Mera and the Mesolcina valleys. Most pegmatites show a simple mineral assemblage consisting of K-feldspar, quartz, and muscovite ± biotite, and only a minor percentage of the dikes (< 5%) contains Sn-Nb-Ta-Y-REE-U oxide, Y-REE phosphate, Mn-Fe-phosphate, Ti-Zr-silicate, Be-Y-REE-U-silicate and oxide minerals (beryl, chrysoberyl, bertrandite, bavenite, and milarite), garnet (almandine-spessartine), tourmaline (schorl to rare elbaite), bismuthinite, magnetite, and rarely dumortierite and helvite. The mineral assemblages, geological context, and chemical compositions allow the distinction between LCT (lithium, cesium, tantalum) and mixed LCT-NYF (niobium, yttrium, fluorine) pegmatites (with only one exception of an NYF dike in the Bodengo area). The LCT pegmatites of the Central Alps did not reach a high degree of geochemical evolution. The most fractionated pegmatites are found in the Codera area and contain Mn-rich elbaite, triplite, pink-beryl, and Cs-Rb-rich feldspar. In the Bodengo area pegmatites locally contain miarolitic cavities and the most evolved pegmatites correspond to the beryl-columbite-phosphate type. From a structural point of view two main types of pegmatites can be distinguished: (1) pegmatites that were involved in ductile deformation and (2) pegmatites that postdated the main ductile deformation of the SSB. Many pegmatites of the Codera valley belong to the first structural type: they were emplaced at relatively high ambient temperature (*ca.* 500 °C) and locally show a pervasive recrystallization of quartz and a mylonitic structure. The Codera dikes trend about 70° and are steeply dipping. In the Bodengo area the main set of pegmatites (trending approximately N–S to NNE–SSW) crosscuts the ductile deformation structures of the SSB, but the area also includes an earlier generation of boudinaged and folded pegmatite dikes. The undeformed pegmatites from this area may contain miarolitic pockets. There is no systematic difference in the mineral assemblage between the two structural types of pegmatites. However, the chemistry of pegmatite minerals, especially of garnet, in addition to field data suggests that the dikes of the Codera and Bodengo areas represent two distinct generations of pegmatites. Structural data and the few existing radiometric ages suggest that pegmatites were emplaced over a time span between 29 and 25 Ma (and possibly as young as 20 Ma), with the youngest dikes postdating the ductile deformations of the Alpine nappes. The present work presents a first comprehensive field description and geochemical – mineralogical characterization of the Alpine pegmatite field of the Central Alps.

*Keywords*: pegmatite, Central Alps, ductile deformation, Bergell pluton

§ *Corresponding author e-mail address*: alessandro.guastoni@unipd.it

## Introduction

The tectonic stack of Alpine metamorphic units (referred to as "nappes" in the Alpine literature) of the Central Alps hosts the largest field of Tertiary (Oligocene–Miocene?) pegmatites of the Alps. This field is sharply delimited to the south by the Periadriatic Line and extends, with a N–S width of over 15 km, for about 100 km from the Ossola valley (to the west) to the Sissone valley (to the east) (Fig. 1a). Pegmatites are abundant in the southern steepened "roots" of the Alpine nappes (Southern Steep Belt, SSB: Studer 1851, Milnes 1974), adjacent to the Periadriatic Fault, and progressively decrease in number towards the north, where the

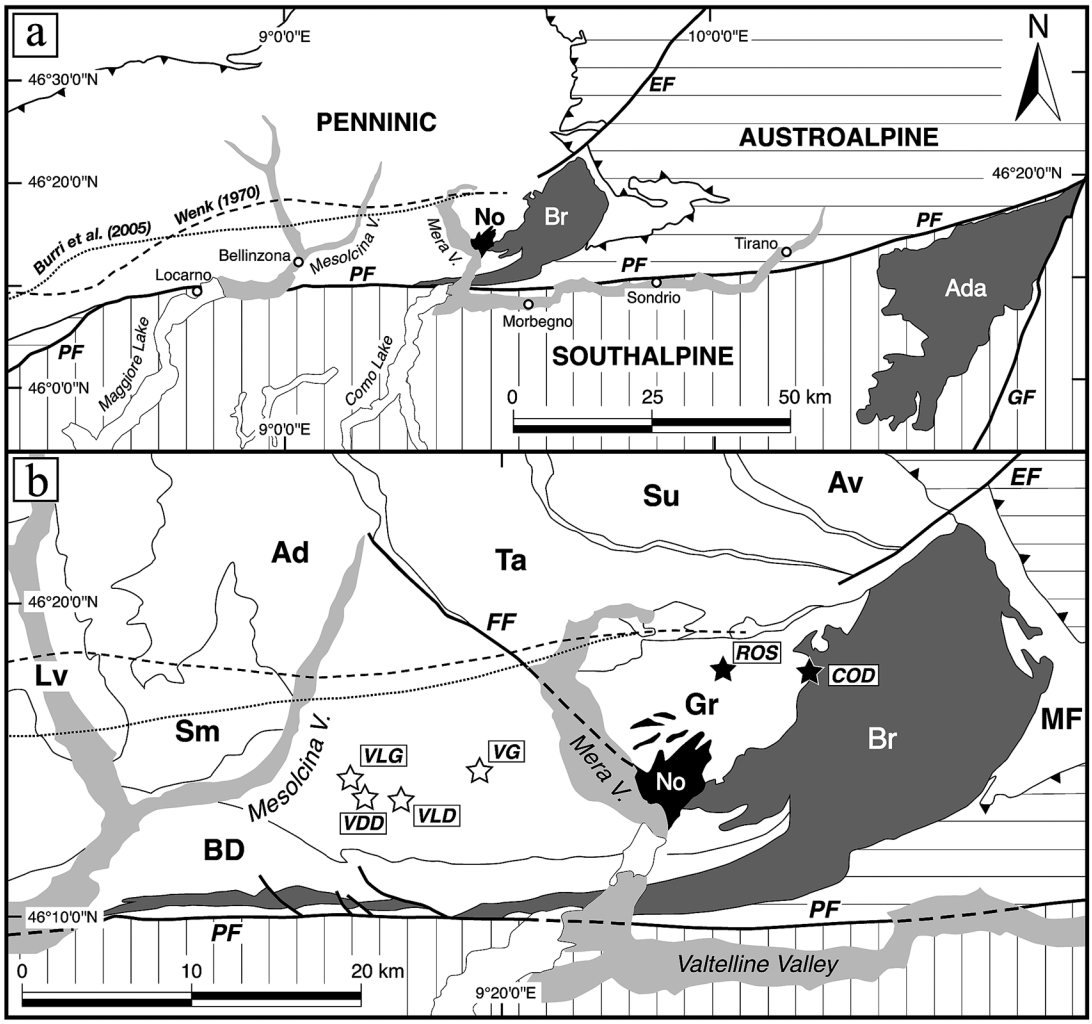


FIG. 1. (a) Simplified structural map of the Central Alps with the field of the Alpine (Oligocene–Miocene?) pegmatites as reported by Wenk (1970) and Burri *et al*. (2005) outlined by dashed and dotted lines, respectively. The map also shows the two major Tertiary batholiths of Adamello (**Ada**) and Bergell (**Br**), in grey, and the smaller and younger Novate stockwork intrusion, in black. The thick black lines represent the Periadriatic Fault (***PF***), the Giudicarie Fault (***GF***), and the Engadine Fault (***EF***). The light grey areas represent quaternary deposits along major valleys. (b) Structural map of the Bergell batholith and the region on the west showing the locations of the Codera and the Bodengo areas. The Codera area includes the upper Codera valley (***COD***) and the Rossaccio locality (***ROS***) indicated with black stars. The Bodengo area includes the Garzelli valley (***VG***), the Darengo valley (***VLD***), the Del Dosso valley (***VDD***), and the Leggia valley (***VLG***) indicated by empty stars. The map also shows the main boundaries (thin black lines) of the Penninic tectonic units: **Lv** = Leventina; **Sm** = Simano; **Ad** = Adula; **Ta** = Tambò; **Su** = Suretta; **Av** = Avers; **BD** = Bellinzona-Dascio; **MF** = Malenco-Forno. The thick black line labeled **FF** is the Forcola Fault.

nappes become flat-lying (Stern 1966, Burri *et al*. 2005) (Fig. 1). The regional boundary of the pegmatite field (which includes associated aplite) was mapped by Wenk (1970) and later by Burri *et al*. (2005) (Fig. 1a). The pegmatite field geographically overlaps (1) the highest-temperature domain of the Barrovian metamorphic dome (Lepontine metamorphic dome), whose isograds are discordant to the nappe boundaries and (2) the zone of Alpine migmatization (whose extent is also reported in the maps of Burri *et al*. 2005 and Wenk 1970). Therefore, in the SSB the leucocratic dikes (including pegmatite and aplite) are often associated with small granitoid bodies (meter to decameter in size) and *in situ* leucosome segregates of the host rock (Burri *et al*. 2005). The interpretation of this structural assemblage is locally difficult due to the occurrence of pre-Alpine leucocratic dikes, migmatites, and granitoids (Hänny *et al*. 1975, Romer *et al*. 1996, Galli *et al*. 2012, 2013). The age of Alpine migmatization and of emplacement of leucocratic dikes in the Central Alps apparently spans approximately the same age bracket as the Tertiary intrusions, whose endmembers are represented by the large Bergell intrusion (32–28 Ma, von Blanckenburg *et al*. 1992, Berger *et al*. 1996, Oberli *et al*. 2004) and the younger and smaller Novate stockwork intrusion (24.0 ± 1.2 Ma, Liati *et al*. 2000). Uranium-Pb dating of monazite from orthogneisses and migmatites from the SSB of the Bodengo valley yielded an age of 23–24 Ma (Hänny *et al*. 1975, Köppel *et al*. 1980), which is slightly older than the Rb-Sr whole rock isochron age of 22 Ma. Along the western boundary of the Bergell pluton, within the Gruf complex, recent SHRIMP U-Pb dating has yielded ages in the range of 34–29 Ma for the outer rim of pre-Alpine zircons (Galli *et al*. 2012). These ages are consistent with field observations that migmatization at 720–740 °C in the Gruf complex was coeval with intrusion of the Bergell pluton (Davidson *et al*. 1996, Berger *et al*. 1996, Galli *et al*. 2012). SHRIMP U-Pb dating of multiple zircon domains from migmatite leucosomes of the SSB close to Bellinzona (Rubatto *et al*. 2009) suggests protracted melting over a time span ranging from 32 to 22 Ma. Gebauer (1996) dated the migmatization event of the SSB within the Cima Lunga nappe at 32.4 ± 1.1 Ma by SHRIMP U-Pb zircon dating; this age indicates that migmatization was coeval with the early phases of the Bergell intrusion. Similarly, in the western part of the pegmatite field, pegmatites intruding amphibolite-facies mylonites of the Simplon ductile shear zone have been dated from 29 to 25 Ma (with a discordant dike as young as 20 Ma) by the U-Pb method applied to monazite and xenotime (Romer *et al*. 1996, Schärer *et al*. 1996). It is noteworthy that Romer *et al*. (1996) distinguished two generations of pegmatite-aplite from the same outcrop at Malesco: (1) the oldest, which intruded along the host-rock foliation and is slightly deformed, yielded an U-Pb age from monazite of 29.2 ± 0.2 Ma; (2) the youngest, which is undeformed and is discordant to the foliation, yielded an U-Pb age from xenotime of 25.5–26.5 Ma. This is consistent with the SHRIMP U-Pb zircon age of 25.1 ± 0.6 Ma obtained for a pegmatite cross cutting the Alpine foliation of the SSB more than 50 km to the east, just north of San Vittore (Gebauer 1996). This age overlaps with the Novate intrusion age determined by Liati *et al*. (2000), who suggested that this pluton, and coeval non-outcropping intrusive bodies, could have been the source of the numerous pegmatites and aplites of the SSB.

If on the regional scale a coincidence between magmatism, migmatization, and pegmatite emplacement is established, on the local scale there is a conspicuous number of pegmatite dikes that apparently postdate the main phase of migmatization and associated ductile deformation. As for the Novate intrusion, in the area between Bellinzona and the Chiavenna valley pegmatites it crosscuts the folds of the Cressim backfolding phase (Nagel *et al*. 2002), which is associated with the steepening of the main nappe foliation and nappe boundaries in the SSB. However, Wenk (1973) noted that, though less deformed than the host Bergell intrusives, pegmatites are locally involved in ductile deformation. He also reported mutual crosscutting relationships between pegmatites and the Novate intrusion, from which he inferred that they were broadly contemporaneous. Galli *et al*. (2013) reported that aplite and pegmatite dikes are present within (and show a weaker ductile overprint than) mylonites (their Fig. 13e), indicating that the emplacement of these dikes was late, but still syntectonic.

Available Rb-Sr and K-Ar ages provide some chronological and temperature constraints on intrusion of pegmatites, though the meaning of these ages in terms of cooling temperature is still debated (*e.g*., Villa 1998). A summary of regional radiometric data is given by Hansmann (1996) and includes data from pegmatites, the Bergell intrusives, and metamorphic rocks. For the western Bergell tonalite, Hansmann (1996, Fig. 6) reconstructed a cooling history (adjusted to an altitude of 1900 m a.s.l.) from magmatic conditions at 28–32 Ma to *ca*. 300 °C (K-Ar of muscovite and Rb-Sr of biotite) at *ca*. 21 Ma. A Rb-Sr muscovite age of 26.3 ± 1 Ma for a pegmatite intruding the Gruf complex in the Piana valley (a tributary of the Codera valley) could record the age of cooling through *ca*. 500 °C. If this assumption is correct, it provides the minimum age of the pegmatites in the area, as well as the minimum temperature for their emplacement. A post-kinematic pegmatite dike from the Bodengo valley (Hänny *et al*. 1975) yielded a Rb-Sr biotite-whole rock age of 19.2 Ma, consistent with the mineral isochron ages of the country metagranitoid gneisses (in the range between 18.4 ± 0.6 and 19.4 ± 0.6 Ma). This fits with the general pattern of biotite ages of the Central Alps (Jäger 1962) and suggests that pegmatites were emplaced before 19 Ma in a host rock

at $T > 300$ °C. This is also consistent with the K-Ar illite age of 19 Ma obtained from a brittle Riedel fault crosscutting the tail of the Bergell pluton (Zwingmann & Mancktelow 2004).

Though the regional extension of the Oligocene pegmatite field of the Central Alps has been described (Wenk 1970, Burri *et al.* 2005), and there are many studies dealing with specific and local aspects of these pegmatites, an attempt to integrate the geochemistry, mineralogy, and field textural and structural features of pegmatites over a regional scale is still missing. With this aim, we have investigated pegmatites in two areas in the central-eastern part of the pegmatite field (Guastoni 2012).

The first area includes two localities, located on the western border of the Bergell pluton: (1) the eastern upper Codera valley (COD locality in Fig. 1b) and (2) the Rossaccio locality (ROS) along the southern divide of the Bergell valley. This area will be referred to as the Codera area in the following text.

The second area covers a large region, including the upper portions of a series of valleys (Garzelli valley, VG; Leggia valley, VLG; Del Dosso valley, VDD; Darengo valley, VLD) located between the Mera (east) and the Mesolcina valleys (west) (Fig. 1b). This area roughly corresponds to the zone studied by Hänny *et al.* (1975) and Nagel *et al.* (2002). Following Hänny *et al.* (1975), this area will be referred to as the Bodengo area throughout the text.

Both the selected areas include locally extensive glacier-polished outcrops that allow the structures to be mapped in detail. The two areas present some contrasting features with regard to the structural features and magmatic texture of the pegmatites. We show in this study that the pegmatites have a similar and characteristic geochemical and mineralogical signature on the regional scale and can be classified as differentiated beryl-columbite-phosphate LCT (lithium, cesium, tantalum) types in the most evolved cases. However, both the field features and the chemistry of pegmatite minerals suggest the existence of two distinct generations of dikes in the two areas.

## Geological Framework and Field Description

### *Codera area*

The eastern side of the upper Codera valley exposes the east-dipping contact between the Bergell pluton and the underlying high-grade country rocks of the Gruf complex (Fig. 1b). This western part of the pluton represents the base of the large lobe forming the main body of the Bergell intrusion, whose upper part is exposed to the east in the Sissone valley due to post magmatic tilting (Davidson *et al.* 1996, Rosenberg 2004), whereas the "root" zone stretches to the west as a thin foliated band parallel to the main foliation in the SSB. The east-west profile across the main body of the Bergell batholith therefore exposes a complete crustal section across a pluton of more than 12 km thickness, with the deepest parts in the west ductilely deformed and folded together with the Gruf unit during the syn-magmatic stages and subsequent postmagmatic cooling (Davidson *et al.* 1996, Rosenberg 2004). The Bergell pluton consists of dominant granites with centimetric phenocrysts of K-feldspar (referred to as "Ghiandone", Balconi 1941) and a relatively thinner outer rim of tonalites (referred to as "Serizzo", Balconi 1941). In the study area tonalites are a few tens of meters thick and show a transitional contact with the granites. The magmatic rocks close to the contact commonly show a solid-state foliation, which is locally strongly developed and subparallel to the pluton boundary.

The pluton contact is crosscut by a swarm of steeply dipping leucocratic dikes (microgranite, aplite, and pegmatite) and quartz veins. Grey quartz commonly forms the core zone of the pegmatite dikes. Field relationships indicate that the microgranite is younger than the pegmatite and commonly was emplaced exploiting earlier pegmatite dikes (Fig. 2a, b). Pegmatites have a thickness of as much as 1 m and commonly preserve pristine igneous textures, including graphic quartz-feldspar intergrowths, graphic black tourmaline and garnet (Fig. 3c,d), comb structures of K-feldspar, and muscovite and biotite radiating aggregates. A small number of dikes contain centimetric prismatic tourmaline and beryl-aquamarine, and mm-sized garnet crystals; these minerals are always completely embedded in quartz or quartz-feldspar (Fig. 3). The main set of pegmatites is steeply dipping (mean dip 75°), both towards north and south, with mean strike about 70° (Fig. 4a). Crosscutting relationships indicate the presence of more than a single generation of pegmatite dikes (Fig. 2c).

The Bergell intrusive rocks show localized ductile shear zones, in addition to the locally pervasive solid-

Fig. 2. Field features of pegmatites in the Codera area. (a) Photomosaic assembled by photogrammetry of a glacier-polished outcrop showing a set of pegmatite dikes (**p**) and a younger set of microgranite dikes (**g**) within the Bergell granitoids. The microgranite dikes crosscut, and locally exploit, the pegmatite dikes. (b) Leucocratic microgranite dike crosscutting and exploiting precursor pegmatite dikes [detail of the outcrop shown in (a)]. Pencil (14.5 cm) for scale. (c) Crosscutting pegmatites. The younger dike crosscut a pegmatite with a core injected by a fine-grained leucocratic granite. View to the north. Pencil (14.5 cm) for scale. (d) Pegmatite dike displaced left-laterally and thinned along a crosscutting ductile shear zone which exploited a precursor joint in the Bergell tonalite. View to the north. Pencil (14.5 cm) for scale. (e) Sheared pegmatite dike with paired ductile shear zones at the boundaries within a granite (Ghiandone) with centimetric K-feldspars. The shear component on the outcrop plane is dextral. View to the NNW. Pencil (14.5 cm) for scale.

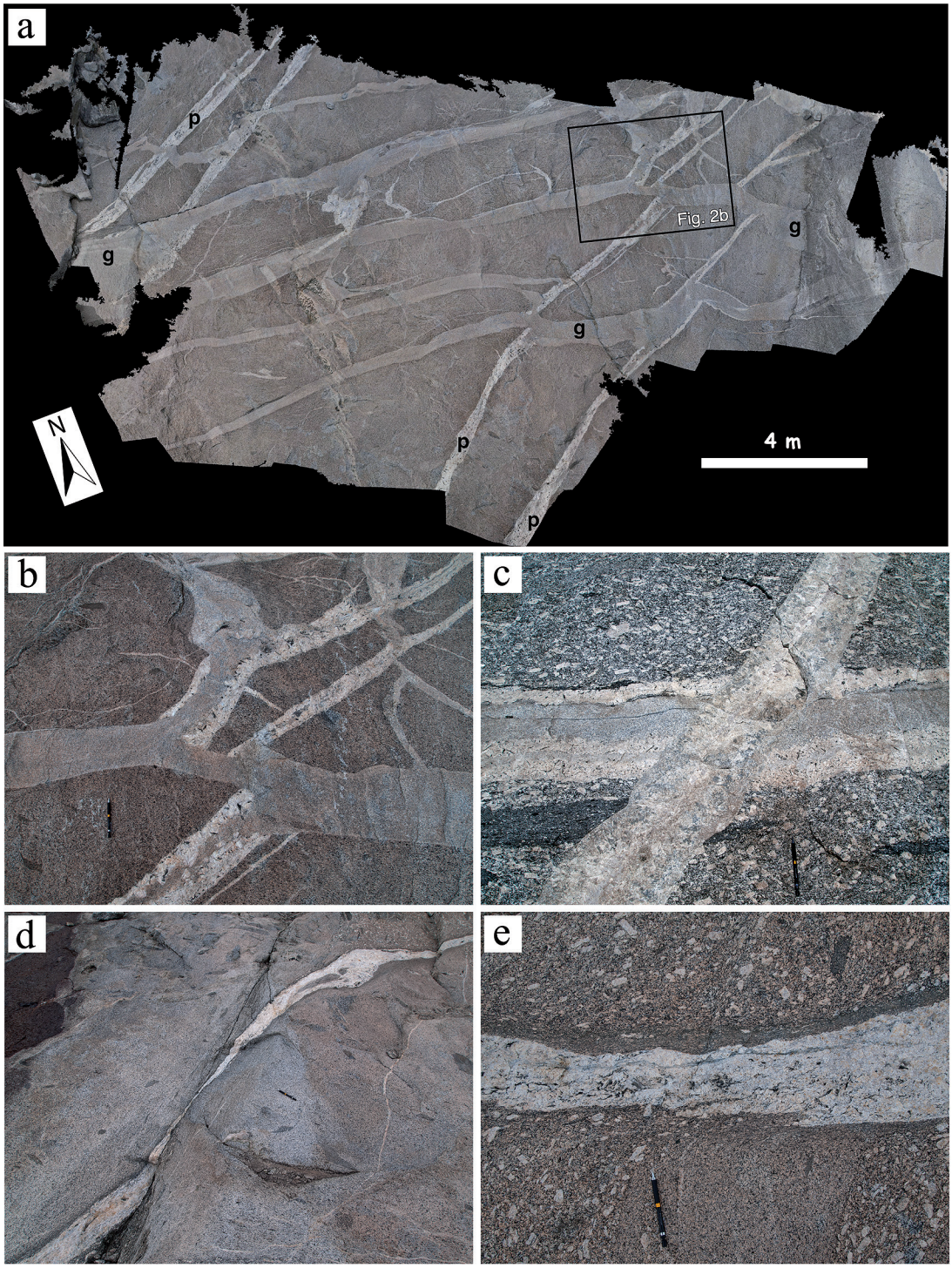
a
p
g
Fig. 2b
g
g
N
p
4 m
p
b
c
d
e

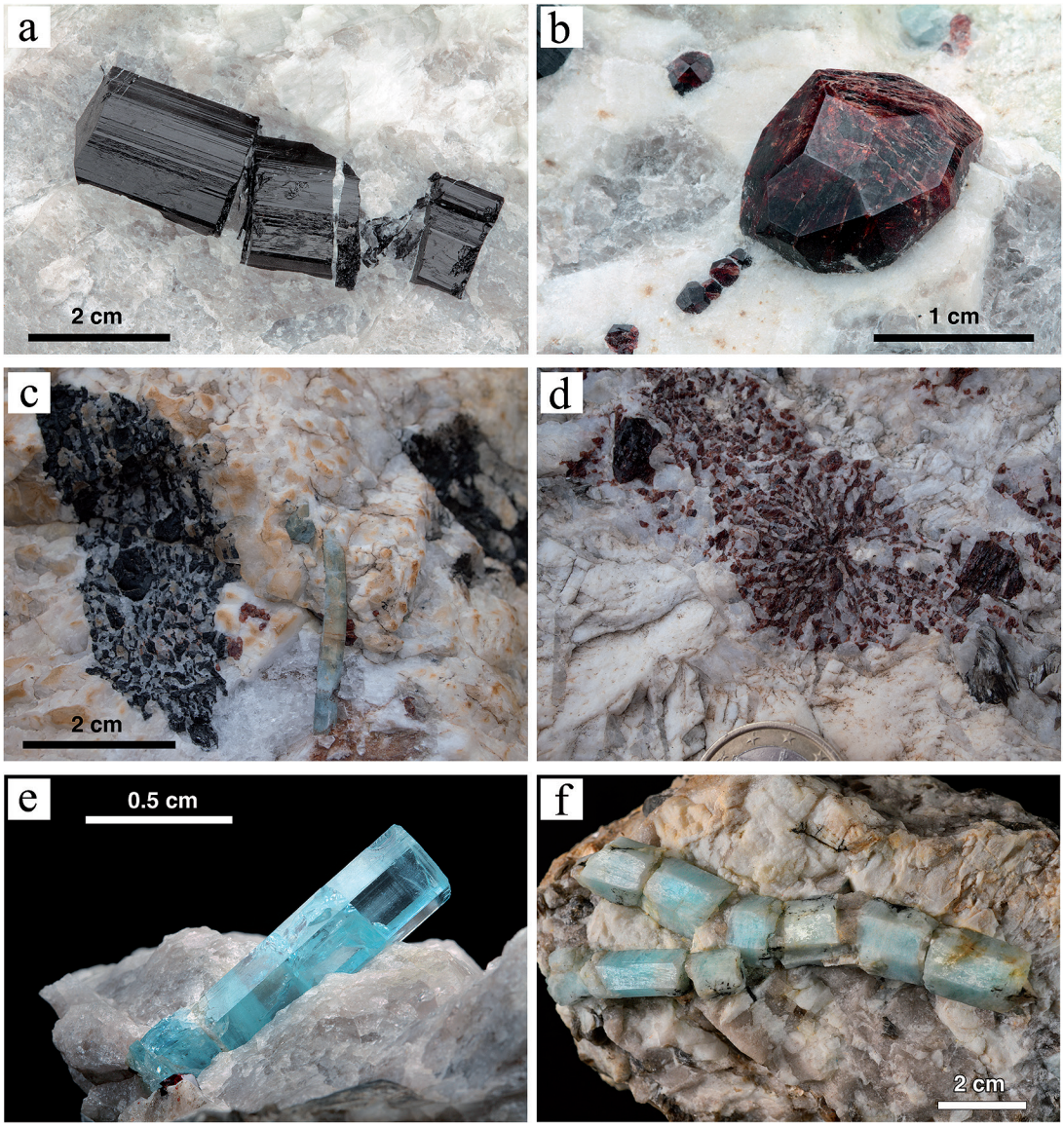


FIG. 3. Pegmatite minerals from the Codera area. (a) Boudinaged black (schorl) tourmaline within quartz; fractures are sealed with quartz. Rossaccio locality. (b) Idimorphic garnets within a quartz-feldspar graphic intergrowth; Rossaccio locality. (c) Graphic black tourmaline and beryl. The beryl is bent and healed. Upper Codera valley. (d) Graphic and small isoblastic garnet from the CODp dike. Coin (1 euro) for scale. (e) Gem-quality beryl (aquamarine); the crystal was freed from the surrounding quartz matrix but was originally completely enclosed. Upper Codera valley. (f) Microboudinaged beryl with the necks filled with quartz. Rossaccio locality.

state foliation, whose orientation is very similar to that of the pegmatites (Fig. 4b). The shear zones have a mineral lineation plunging in the range of 20 to 50°, and the sense of shear indicators indicate transpressive kinematics. The shear zones exploited high-temperature joints (Fig. 2d) and compositional boundaries, including pegmatite dikes (Fig. 2e), as described for ductile deformation developed during post-magmatic cooling of many other plutons (*e.g.*, Pennacchioni 2005, Pennacchioni & Zucchi 2013). This is consistent with

the general observation that planar compositional or structural heterogeneities localize shear deformation in an isotropic rock (Pennacchioni & Mancktelow 2007, Mancktelow & Pennacchioni 2013). Many pegmatites (but also the leucocratic microgranite dikes) distinguished in the stereoplot of Figure 4c show the effect of ductile deformation. Some pegmatites were just dragged into the mylonitic shear zones (Fig. 2d), but more commonly pegmatite and leucocratic dikes localized the deformation and developed mylonitic shear zones at their boundaries (paired shear zones *sensu* Mancktelow & Pennacchioni 2005) (Fig. 2e) or an internal foliation, particularly in dikes showing a quartz core. Though some dikes appear in the field to preserve the pristine magmatic structure, the effects of an incipient ductile deformation are evident from microboudinage of tourmaline and beryl (Fig. 3a,f) or from healed bent crystals (Fig. 3c). Quartz veins oriented parallel to the main set of pegmatites are commonly transformed to quartz mylonites. A ductile deformation of pegmatites is observed both inside the pluton and within the Gruf unit, with a strong mylonitic overprint of pegmatites present within the Gruf units in the Rossaccio locality.

*Bodengo area*

The rocks outcropping in this area mainly belong to the Penninic Adula and Simano nappes, which have a heterogeneous composition but largely consist of high-grade orthogneiss, paragneisses, felsic migmatites, and minor metamorphosed mafic and ultramafic rocks, with common evidence of migmatization. These rocks were affected by polyphase metamorphism and deformation. The three main ductile deformation phases (D1-D3) all developed under high grade conditions (600–750 °C, Nagel *et al*. 2002). The D3 phase is related to the steepening of the S1-S2 foliation to the south in the SSB. In the study area, D3 is represented by major, km-scale folds (*e.g*., Paglia antiform; Kopp 1923, Brüggmann 1965; Cressim antiform, Kopp 1923), that can be traced for a few tens of kilometers along axis, and are associated with minor folds at the outcrop scale showing a mineral lineation parallel to the fold axis, but commonly without a well-developed axial plane foliation. During the D3 phase the felsic gneisses underwent migmatization (Hüber 1993).

Pegmatites are widespread over the whole area, forming swarms of subparallel dikes with a spacing on

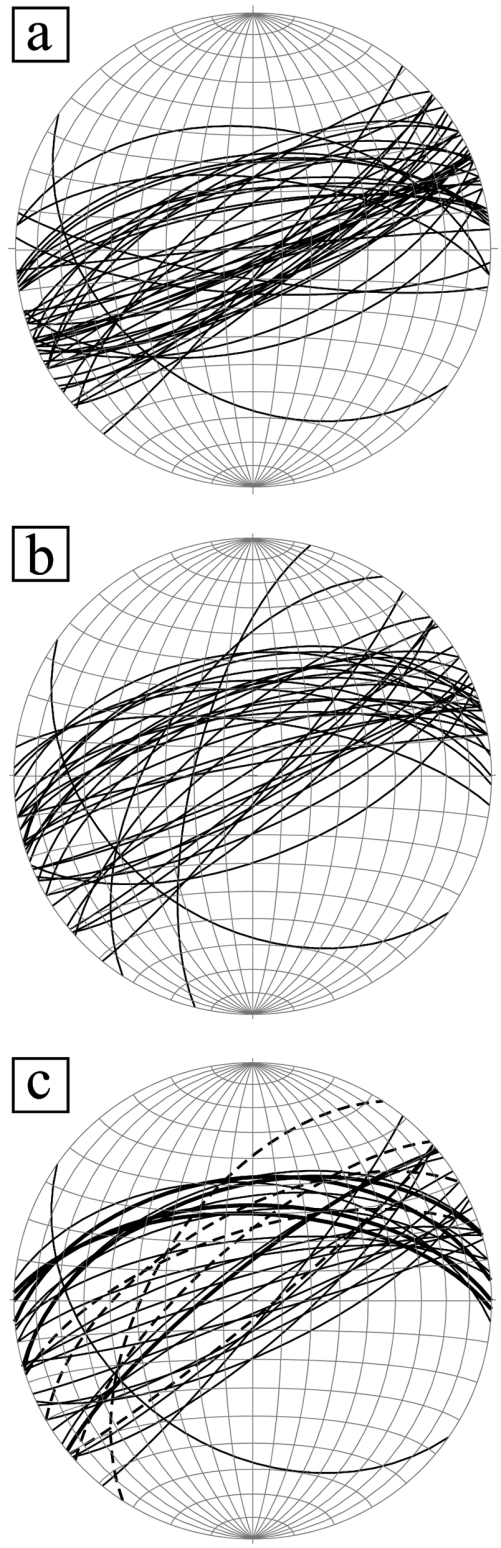


FIG. 4. Stereographic plots (lower hemisphere, equal area) of the orientations of the pegmatite dikes (a), mylonites (b), and ductilely deformed dikes and veins (c) from the upper eastern Codera valley. In (c) the thin lines represent pegmatites, thick lines are leucocratic (microgranite) dikes, and dashed lines indicate quartz veins.

the order of tens of meters, as is visible on the eastern cliff of the Pizzo Paglia (Fig. SOM1, available from the Depository of Unpublished Data on the MAC website, document CM52_191). The main set of pegmatites dips W to WNW from moderately (mean angle of 45–50° in the Darengo, Del Dosso, and Leggia valleys) to steeply (mean angle of 70° in the Garzelli valley) (Fig. 5). These pegmatites have a thickness of as much as a few meters, but more commonly are a few decimeters thick or less. The thickest dikes can extend for hundreds of meters. In general, these pegmatites do not show effects of ductile deformation and crosscut the D3 folds of the country rocks (Fig. 6a), but some dikes have sheared boundaries with the development of a S-C foliation delineated by white mica (Fig. SOM2, available from the Depository of Unpublished Data on the MAC website, document CM52_191). The main set of pegmatites crosscuts an earlier set oriented at a small angle to the host rock

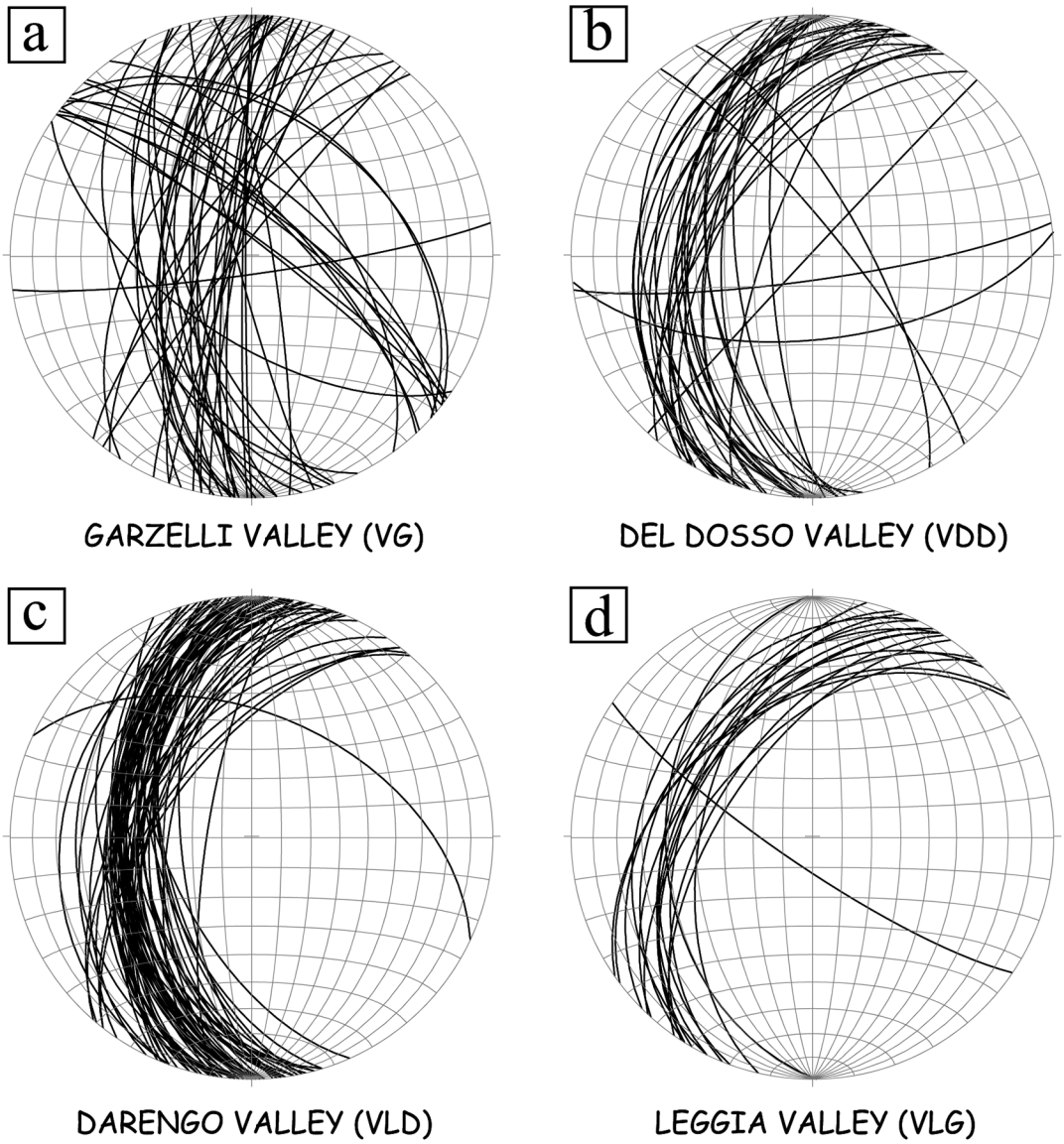


FIG. 5. Stereographic plots (lower hemisphere, equal area) of the orientations of pegmatite dikes from different localities (see Fig. 1 for location) of the Bodengo area.

foliation (Fig. 6b, c), but still discordant to it, which in the Garzelli and Del Dosso valleys dip steeply towards the NE (mean orientation: 68°/044°) (Figs. 5a, b). These earlier dikes were ductilely deformed and show boudinage (Fig. 6c), buckling, and shearing.

Pegmatites from the Bodengo area show the same textures as described for the Codera area (*e.g.*, comb structures, Fig. 6d) and locally developed a zoned texture, which is commonly symmetric, except for the presence, in some cases, of a fine-grained layered zone at the bottom of the dike (line rock *sensu* Webber *et al*. 1997) composed of K-feldspar, albite, quartz, and muscovite. Zoned pegmatites include: (1) an outer layer of centimetric K-feldspar, albite, muscovite, and quartz; (2) an intermediate layer of coarser (a few cm to dm in size) graphic quartz/K-feldspar intergrowth, albite, muscovite, pale blue beryl, graphic black schorl, and mm-sized garnets; and (3) a core zone developing a giant texture (up to metric perthitic K-feldspar), sporadically including miarolitic cavities (Fig. 6e). These miarolitic cavities contain brownish to smoky vitreous quartz (Fig. 7a), aquamarine beryl (Fig. 7b), schorl tourmaline, garnet, and rare greyish mm-size zircon crystals or wodginite (Fig. 7c). Miarolitic cavities occur either as isolated large pockets (up to 1 m in size, Fig. 6e) or as smaller (pluridecimetric) pockets aligned subparallel to the dike boundaries on the upper side of the core zone (Guastoni 2012). Miarolitic pegmatites do not show comb textures.

The leucocratic gneiss of the Bodengo area contains abundant quartz veins which in most cases were involved in the D3 deformation, developing buckled folds or filling gaps related to foliation boudinage of the main schistosity. However, some quartz veins trend subparallel to the main set of pegmatites as described for the Codera area and appear to have been emplaced during the same event as the pegmatites. In the Del Dosso valley one of these veins is up to a few meters in thickness and is undeformed; this contrasts with the strong mylonitic overprint of many quartz veins from the Codera area.

## Microstructure of Ductile Shear Zones of the Codera Area

In the Codera area, ductile deformation of pegmatites is common. We have sampled tonalite mylonites flanking sheared dikes, and quartz mylonites derived from quartz-rich dikes subparallel to the main set of pegmatites. Sampling was aimed at placing some constraints on the temperature of pegmatite emplacement and deformation. The stable mineral assemblage along the mylonitic foliation consists of quartz, biotite, plagioclase, epidote, ±K-feldspar. The mylonites show dynamic recrystallization of quartz, biotite, and feldspar. The magmatic biotite recrystallized to lighter colored, brown to locally green-pleocroic biotite forming the matrix of the mylonites. Both K-feldspar and plagioclase were transformed to ultrafine-grained (grain size of a few microns) aggregates (Fig. 8a). The K-feldspar is locally replaced by fine-grained myrmekites that underwent recrystallization along high strain zones and evolved to aggregates of polygonal quartz-plagioclase. Typically, K-feldspar and plagioclase remain as numerous rounded porphyroclasts in high-strain rocks and show tails of recrystallized aggregates (Fig. 8b). Quartz mylonites, developed from almost pure quartz veins and from the quartz cores of pegmatites, consist of recrystallized aggregates of small (commonly < 50 μm) grains of equant to slightly elongate shape (defining a shape preferred orientation oblique to the main foliation, Fig. 8c). Under crossed polars the recrystallized aggregates have a dominant dark color or show an extinction banding (Fig. 8c). The microstructure and the mineral assemblage are similar to those of mylonites and quartz mylonites typically developed during the stages of postmagmatic cooling of granitoid plutons (Pennacchioni 2005, Pennacchioni & Zucchi 2013).

## X-ray Texture Goniometry

The Crystallographic Preferred Orientation (CPO) of three samples (12-144A, 12-144B and 12-166) of quartz mylonites from the Codera valley was determined by X-ray texture goniometry (TG). Details on this technique can be found in the Appendix.

The experimental pole figures for {110}, {112}, and {201}, and the calculated pole figures for {001} are shown in Figure 9. The three investigated samples all show a CPO, which is particularly strong in samples 12-144A and 12-144B. The *c*-axis pole figures are characterized by a strong maximum centered on the Y axis (12-144A and 12-144B) or by a partial Y-Z girdle centered on the Y axis that is slightly asymmetric to the foliation plane, with the asymmetry reflecting the sense of shear (12-166). The {110} pole figure is also slightly asymmetric with the strongest <*a*> axis maxima rotated synthetically with the sense of shear with respect to the shear plane. This type of CPO is almost identical to the CPO of mylonitic quartz veins associated with mylonites within the Tertiary Adamello pluton (Pennacchioni *et al*. 2010).

## Mineral Assemblage of the Alpine Pegmatite

### *Historical overview*

There is a long history of mineralogical studies of the Alpine pegmatites of the Central Alps. The occurrence of beryl and columbite in pegmatites of the Vigezzo valley was first reported by Spezia (1882) and by Strüver (1885), respectively. Zambonini (1907, 1908) discovered two new minerals in the pegmatites of the Vigezzo valley: (1) strüverite, (Ti, Ta, Fe)$O_2$

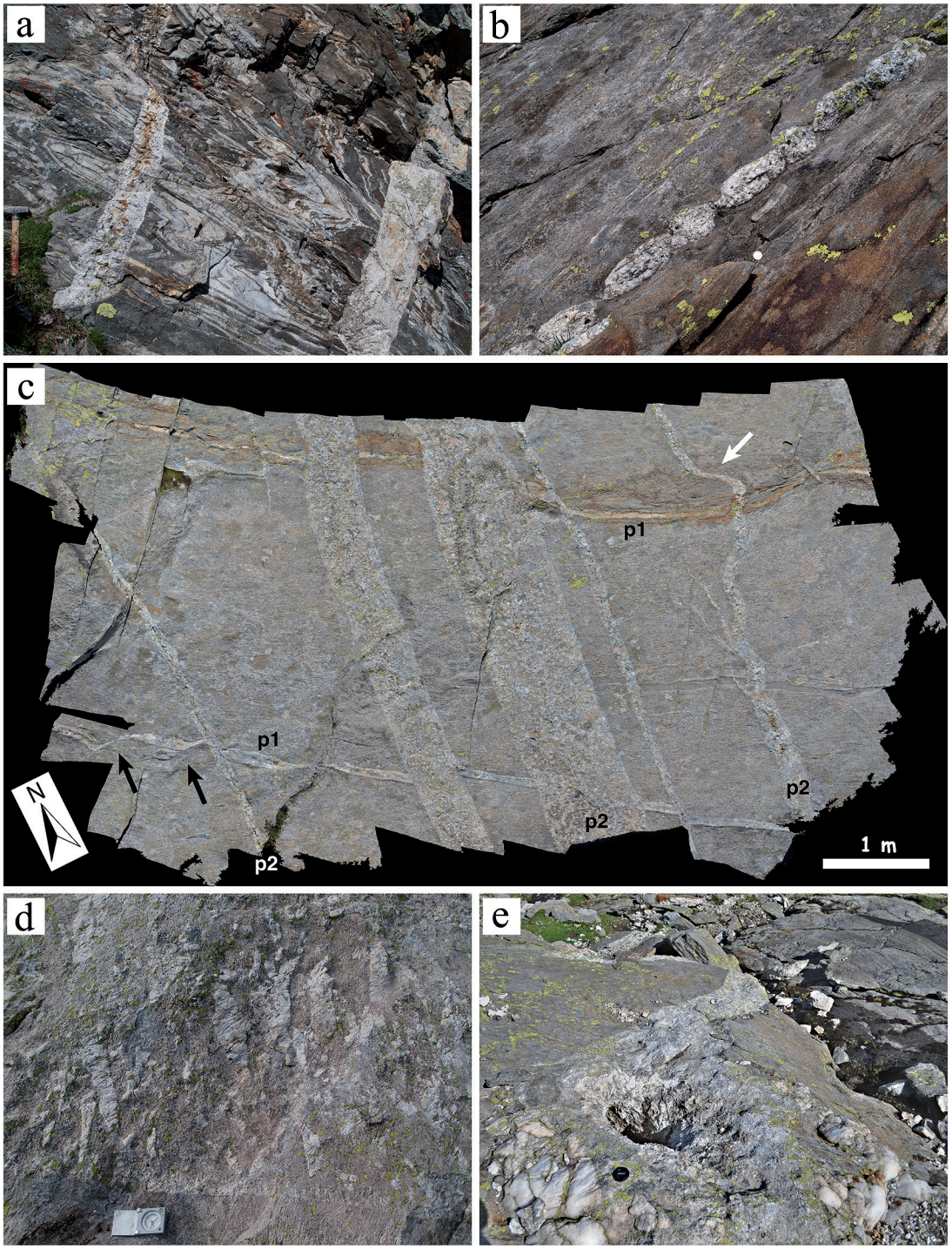


FIG. 6. Field features of pegmatites in the Bodengo area. (a) Pegmatites of the main set crosscutting the foliation and D3 folds within amphibolites of the SSB. Del Dosso valley; hammer (40 cm length) for scale. (b) Pinch-and-swell boudinage of a pegmatite oriented at a small angle to the main foliation of the SSB. This boudinaged dike is crosscut by the main set

(later redefined as Nb-rich rutile), and (2) delorenzite, (Y, Ce, Ca)(Ta, Nb, Ti)$_2$(O,OH)$_6$ (later renamed tanteuxenite). Taddei (1940) described the mineralogy of pegmatites of the Calanca and Mesolcina valleys, Switzerland. Gramaccioli (1958) reported delorenzite from Craveggia, and Roggiani (1966) first described the albitized pegmatite of Alpe Rosso (Vigezzo valley). Aquamarine, garnet crystals, and other rare minerals (columbite- and euxenite-group minerals, zircon) were reported in the pegmatites of the Codera valley by Peco (1949) and by De Michele (1970). Zhang *et al*. (2001) analyzed graphic garnet from the Codera valley for which they reported a composition of almandine$_{27–37}$ spessartine$_{53–68}$ pyrope$_{3–4.5}$.

*Mineral assemblages and chemistry*

Most pegmatites have a simple mineral assemblage consisting of K-feldspar, quartz, muscovite ± biotite. Only a very minor number of pegmatites contain: (1) Sn-Nb-Ta-Y-REE-U oxide minerals, (2) Y-REE phosphate minerals, (3) Mn-Fe-phosphate minerals, (4) Ti-Zr-silicate minerals, (5) Be-Y-REE-silicate and oxide minerals (beryl, chrysoberyl, bertrandite, bavenite, and milarite), (6) garnet (almandine-spessartine), (7) tourmaline (mainly schorl with a rare occurrence of elbaite and foitite), and (8) rare dumortierite, helvite, and microlite (Guastoni *et al*. 2004). Except for the rare occurrences of elbaite, dumortierite, and helvite in the Codera area, and tapiolite-Fe (Guastoni & Demartin 2003) and wodginite (Guastoni 2012) in the Bodengo area, the mineral assemblage of most of these non-barren pegmatites is remarkably constant, containing almandine-spessartine, schorl, and beryl (Guastoni 2012). There is no systematic or notable change in mineral content of pegmatites of the Codera area compared with those of the Bodengo area, despite

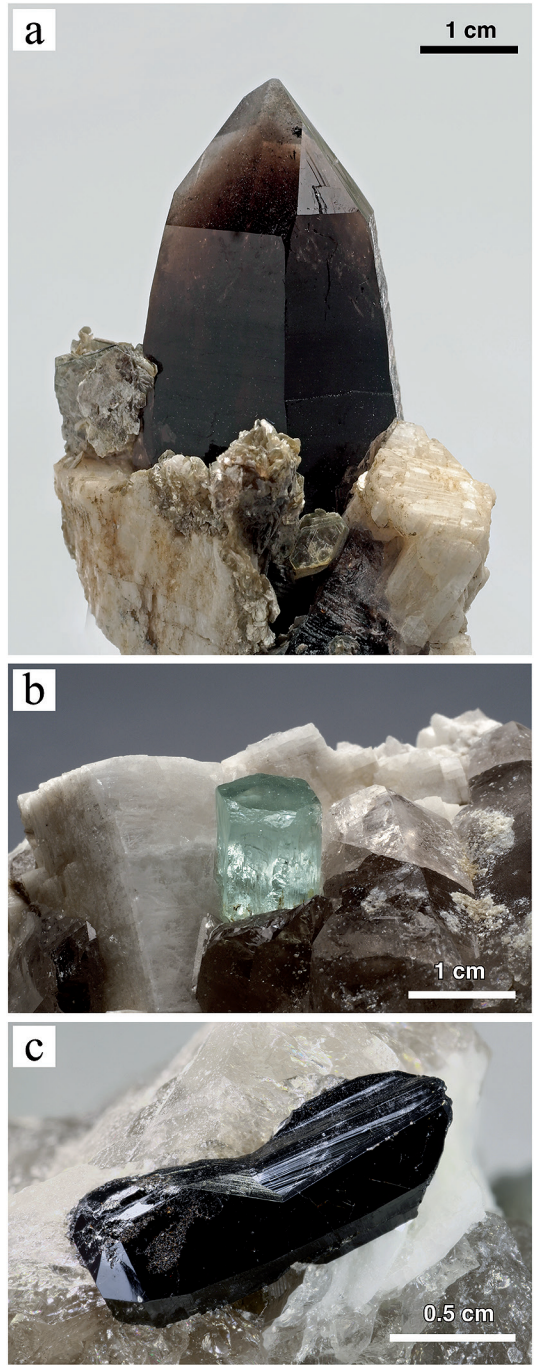


FIG. 7. Pegmatite minerals from miarolitic cavities of the Bodengo area. (a) Smoky quartz with microcline and muscovite. (b) Terminated gem-quality beryl (aquamarine). (c) Twinned crystal of wodginite.

of undeformed pegmatites of the area. Del Dosso valley; coin (1 Euro) for scale. (c) Photomosaic assembled by photogrammetry of a glacier-polished outcrop showing two intersecting sets of pegmatites with the older thin dikes (**p1**) deformed along ductile shear bands (indicated by black arrows in the lower left part of the outcrop); the younger dikes (**p2**) crosscut at a high angle the host-rock foliation and appear mainly undeformed except for showing locally a ductile overprint (as indicated by the white arrow in the upper right part of the outcrop). (d) Pegmatite of the main set of dikes crosscutting the main foliation of the country leucocratic gneisses (lower part of the photograph) showing elongated K-feldspar crystals oriented approximately orthogonal to the dike boundary (comb structure). Garzelli valley; compass for scale. (e) Miarolitic cavity in a pegmatite dike. The presence of the cavity is associated with a swelling of the pegmatite dike. Leggia valley; camera lens cap (6 cm in diameter) for scale.

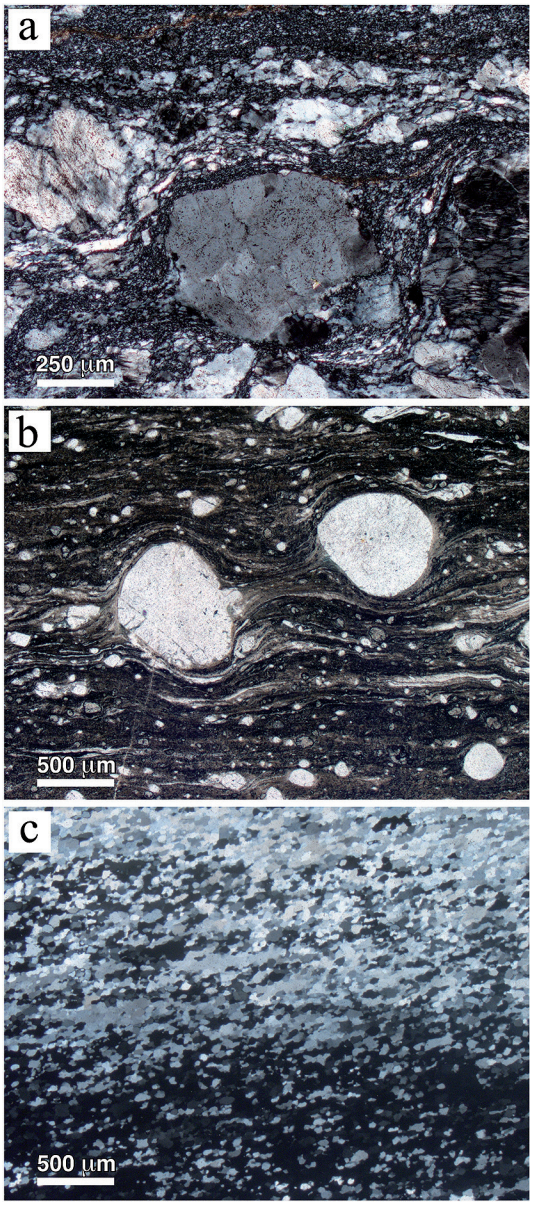


FIG. 8. Deformation microstructures of the Codera mylonites (optical microscope photographs). (a) Porphyroclasts of K-feldspar wrapped around by an aggregate of ultra fine-grained plagioclase-quartz ± K-feldspar defining an S-C asymmetric foliation. Crossed polars. (b) Rounded feldspar porphyroclasts in an ultra fine-grained biotite-rich matrix of a tonalite mylonite. Parallel polars. (c) Dynamically recrystallized aggregate in a quartz mylonite showing extinction banding under crossed polars. In all of the photographs the sense of shear is dextral.

the differences in pegmatite texture (*e.g.*, the presence of miarolitic cavities in the latter, which are absent in the former), in deformation (relatively common ductile overprint in the Codera area *versus* mostly undeformed pegmatites in the Bodengo area), and orientations of dikes. These non-trivial minerals are commonly present as scattered occurrences along dikes, which otherwise appear as barren-type pegmatites. It is of note that, in the Codera area, tourmaline-beryl-garnet pegmatites are found within the intrusive rocks close to the contact but disappear further inside the pluton, where the same set of dikes consists of aplites and feldspar (ceramic) pegmatites. These latter contain only K-feldspar and minor muscovite-biotite (Guastoni 2012).

The chemical composition of selected mineral phases was determined using a CAMECA SX-50 electron microprobe. Details on the analytical technique can be found in the Appendix. The analyzed minerals came from selected dikes which have been labeled accordingly with their location using the acronyms of Figure 1b (*e.g.*, COD, VLG, *etc.*); lower case letters and numbers after the upper case label distinguish different dikes from the same locality. The pegmatite samples from the Codera area include: CODg, CODp (phosphate-bearing) (from the upper Codera valley), and ROSS (from Rossaccio). The pegmatite samples from the Bodengo area include: VDD (Dosso valley), VLGa, VLGb, and VLGm (Leggia valley), and VG (Garzelli valley). A leucocratic gneiss forming the host rock of pegmatite and containing tourmaline was also sampled at Pizzo Paglia (sample PP) in the Leggia valley of the Bodengo area.

*Niobium-tantalum-yttrium-rare earth elements (REE)-uranium oxide minerals.*

Columbite-(Fe) from the CODg dike (Table 1) occurs as black, metallic, tabular to platy crystals as long as 2 cm embedded in K-feldspar. Columbite-(Fe) from sample G2 contains as much as 69.8 wt.% $Nb_2O_5$ in the core and *ca.* 66.5 wt.% in the rim. Columbite-(Fe) incorporates $WO_3$ (up to 1.20 wt.%), $SnO_2$ (up to 0.28 wt.%), and $UO_2$ (up to 0.81 wt.%). Columbite contains $Y_2O_3$ (0.05–0.10 wt.%), $Nd_2O_3$ (0.05–0.08 wt.%), and $Gd_2O_3$ (0.05–0.10 wt.%). Columbite-(Fe) of sample G3 contains up to 68 wt.% $Nb_2O_5$ in the core and 66 wt.% in the rim. Columbite-(Fe) incorporate $WO_3$ (up to 1.20 wt.%), $SnO_2$ (up to 0.34 wt.%), and $UO_2$ (up to 0.30 wt.%).

Uranium-rich euxenite-(Y) and euxenite-(Y) from the CODg dike (Table 2) occur as black, reddish-brown, platy or prismatic crystals up to 1 cm in length, with conchoidal vitreous fracture, embedded in K-feldspar. Sample G1 consists of U-rich euxenite-(Y) and is rather heterogeneous in composition. The core contains $Nb_2O_5$

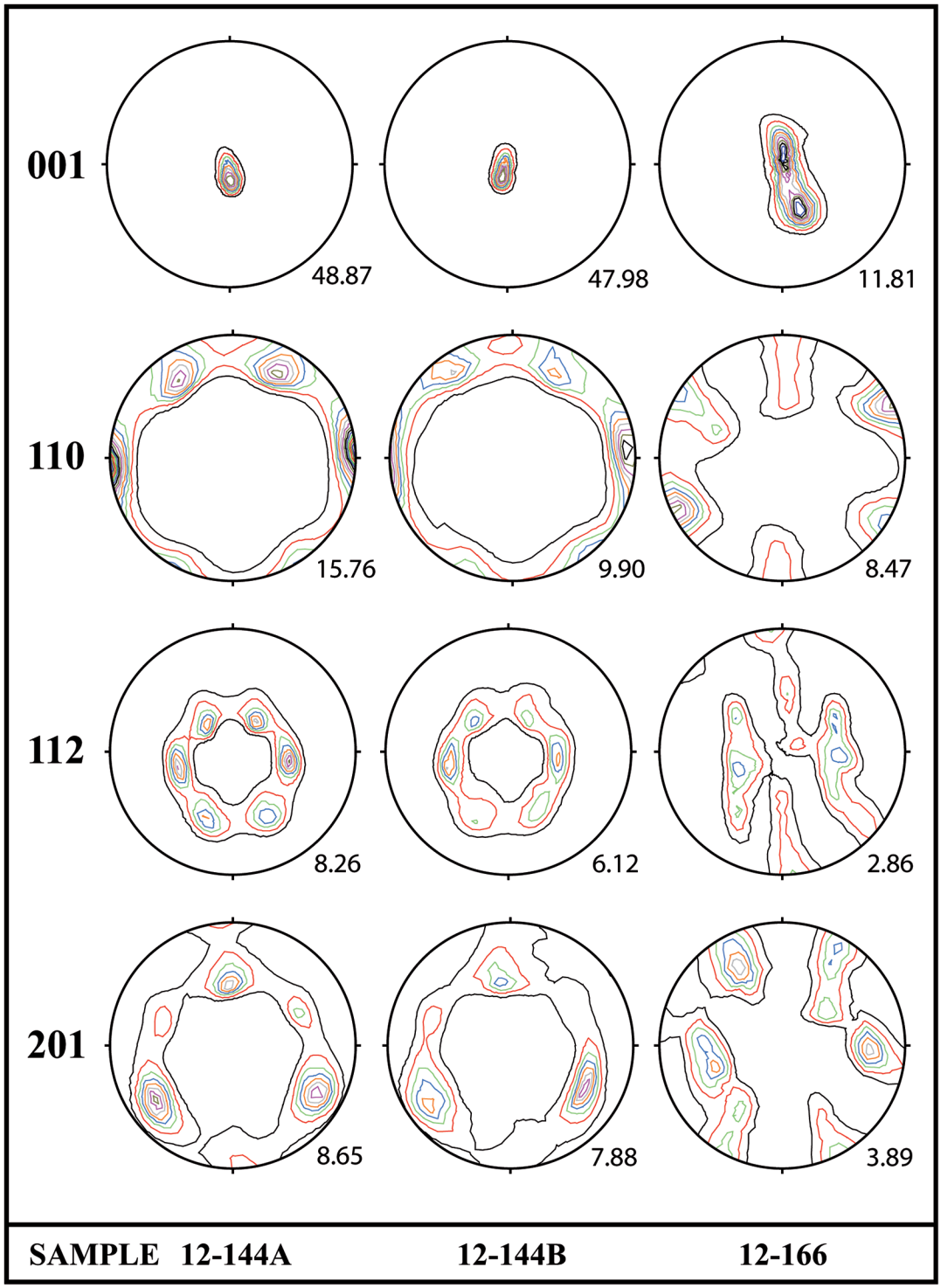


FIG. 9. Plots (upper hemisphere, equal area ) of (001) (*c* axis), (110) (<*a*> axis), (112), and (201) axes of quartz mylonites of the Codera area determined by texture goniometry. The plots are cumulative and the total investigated area in each sample is 2 $cm^2$.

up to 37.3 wt.%, $UO_2$ up to 20.82 wt.%, and $Y_2O_3$ up to 6.74 wt.%. The crystal rim contains $Nb_2O_5$ up to 34.97 wt.%, $UO_2$ up to 15.87 wt.%, and $Y_2O_3$ up to 8.58 wt.%. Sample G1 is enriched in LREE and HREE and contains minor amounts of $SnO_2$ (up to 1.34 wt.%) and $WO_3$ (up to 1.80 wt.%). Sample G4 consists of euxenite-(Y) and is rather homogenous in composition. The core of the crystal contains up to 37.45 wt.% $Nb_2O_5$, up to 11.65 wt.% $UO_2$, and up to 9.97wt.% $Y_2O_3$. The crystal rim contains up to 34.94 wt.% $Nb_2O_5$, up to 10.82 wt.% $UO_2$, and up to 10.12 wt.% $Y_2O_3$. Sample G4 is also enriched in LREE and HREE and contains minor $SnO_2$ (up to 1.99 wt.%) and $WO_3$ (up to 1.85 wt.%). The highly metamict state of the crystal does not allow sufficient diffraction peaks to be determined for reliable cell data.

Wodginite is a Ta, Sn oxide which is a proxy for a high level of Nb-Ta fractionation in pegmatites of the REL-Li. In the VLGb dike (Table 3) this mineral was found in miarolitic pockets as black, metallic, barrel-

TABLE 1. MICROPROBE COMPOSITIONS OF COLUMBITE-(Fe) FROM THE CODg DIKE (UPPER CODERA VALLEY)

| Oxide (wt.%) | G2 rim | G2 int | G2 core | G2 core | G3 rim | G3 rim | G3 int-dark | G3 core |
|---|---|---|---|---|---|---|---|---|
| MgO | 0.24 | 0.24 | 0.21 | 0.14 | 0.33 | 0.30 | 0.32 | 0.23 |
| CaO | 0.00 | 0.00 | 0.00 | 0.00 | 0.00 | 0.00 | 0.00 | 0.00 |
| $TiO_2$ | 5.44 | 5.32 | 4.55 | 3.74 | 5.54 | 3.27 | 6.51 | 4.10 |
| $Sc_2O_3$ | 1.11 | 1.08 | 0.93 | 0.83 | 0.81 | 0.84 | 0.80 | 0.45 |
| MnO | 7.74 | 7.56 | 7.88 | 8.94 | 4.55 | 6.27 | 4.61 | 6.56 |
| FeO | 11.54 | 11.57 | 11.31 | 10.03 | 14.46 | 13.68 | 13.14 | 12.53 |
| $Y_2O_3$ | 0.09 | 0.10 | 0.06 | 0.05 | 0.00 | 0.00 | 0.00 | 0.00 |
| $Nb_2O_5$ | 66.52 | 67.45 | 68.29 | 69.83 | 61.02 | 66.08 | 65.26 | 67.99 |
| $SnO_2$ | 0.28 | 0.26 | 0.19 | 0.13 | 0.29 | 0.19 | 0.34 | 0.17 |
| $Ta_2O_5$ | 4.86 | 4.90 | 5.06 | 5.24 | 11.58 | 9.44 | 5.20 | 7.25 |
| $WO_3$ | 1.11 | 0.80 | 1.20 | 0.70 | 1.11 | 0.21 | 1.20 | 0.40 |
| $Nd_2O_3$ | 0.00 | 0.08 | 0.06 | 0.05 | 0.00 | 0.00 | 0.00 | 0.00 |
| $Sm_2O_3$ | 0.00 | 0.00 | 0.00 | 0.00 | 0.00 | 0.00 | 0.00 | 0.00 |
| $Gd_2O_3$ | 0.05 | 0.10 | 0.09 | 0.05 | 0.00 | 0.00 | 0.00 | 0.00 |
| $Dy_2O_3$ | 0.00 | 0.00 | 0.00 | 0.00 | 0.00 | 0.00 | 0.00 | 0.00 |
| $Yb_2O_3$ | 0.00 | 0.00 | 0.00 | 0.00 | 0.00 | 0.00 | 0.00 | 0.00 |
| $ThO_2$ | 0.00 | 0.00 | 0.00 | 0.00 | 0.00 | 0.00 | 0.00 | 0.00 |
| $UO_2$ | 0.81 | 0.80 | 0.22 | 0.20 | 0.29 | 0.09 | 0.30 | 0.25 |
| Total | 99.79 | 100.26 | 100.05 | 99.93 | 99.98 | 100.37 | 97.68 | 99.93 |
| | | | | | | | | |
| Mg | 0.020 | 0.020 | 0.018 | 0.012 | 0.028 | 0.026 | 0.027 | 0.020 |
| Ca | 0.000 | 0.000 | 0.000 | 0.000 | 0.000 | 0.000 | 0.000 | 0.000 |
| Ti | 0.231 | 0.225 | 0.193 | 0.159 | 0.241 | 0.141 | 0.280 | 0.175 |
| Sc | 0.055 | 0.053 | 0.046 | 0.041 | 0.041 | 0.042 | 0.040 | 0.022 |
| Mn | 0.370 | 0.360 | 0.376 | 0.428 | 0.223 | 0.304 | 0.223 | 0.316 |
| Fe | 0.545 | 0.544 | 0.533 | 0.474 | 0.698 | 0.656 | 0.629 | 0.596 |
| Y | 0.003 | 0.003 | 0.002 | 0.002 | 0.000 | 0.000 | 0.000 | 0.000 |
| Nb | 1.699 | 1.714 | 1.740 | 1.784 | 1.593 | 1.712 | 1.689 | 1.749 |
| Sn | 0.006 | 0.006 | 0.004 | 0.003 | 0.007 | 0.004 | 0.008 | 0.004 |
| Ta | 0.075 | 0.075 | 0.078 | 0.081 | 0.182 | 0.147 | 0.081 | 0.112 |
| W | 0.016 | 0.012 | 0.018 | 0.010 | 0.017 | 0.003 | 0.018 | 0.006 |
| Nd | 0.000 | 0.002 | 0.001 | 0.001 | 0.000 | 0.000 | 0.000 | 0.000 |
| Sm | 0.000 | 0.000 | 0.000 | 0.000 | 0.000 | 0.000 | 0.000 | 0.000 |
| Gd | 0.001 | 0.002 | 0.002 | 0.001 | 0.000 | 00.00 | 0.000 | 0.000 |
| Dy | 0.000 | 0.000 | 0.000 | 0.000 | 0.000 | 0.000 | 0.000 | 0.000 |
| Yb | 0.000 | 0.000 | 0.000 | 0.000 | 0.000 | 0.000 | 0.000 | 0.000 |
| Th | 0.000 | 0.000 | 0.000 | 0.000 | 0.000 | 0.000 | 0.000 | 0.000 |
| U | 0.010 | 0.010 | 0.003 | 0.003 | 0.004 | 0.001 | 0.004 | 0.003 |
| **Cation Sum** | 3.031 | 3.026 | 3.014 | 2.999 | 3.034 | 3.036 | 2.999 | 3.003 |
| Y+REE | 0.004 | 0.007 | 0.005 | 0.004 | 0.000 | 0.000 | 0.000 | 0.000 |
| Nb+Ta+Ti+W | 2.021 | 2.026 | 2.029 | 2.034 | 2.033 | 2.003 | 2.068 | 2.042 |
| Mn/(Mn+Fe) | 0.404 | 0.398 | 0.414 | 0.474 | 0.242 | 0.317 | 0.262 | 0.346 |
| Ta/(Ta+Nb) | 0.042 | 0.040 | 0.043 | 0.043 | 0.102 | 0.079 | 0.046 | 0.060 |

Structural formula based on 6 oxygen atoms.

TABLE 2. MICROPROBE COMPOSITIONS OF U-RICH EUXENITE-(Y) AND EUXENITE-(Y) FROM THE CODg DIKE (UPPER CODERA VALLEY)

| Oxide (wt.%) | G1 patches U-rich euxenite-(Y) | G1 U-rich euxenite-(Y) | G4 core euxenite-(Y) | G4 intermed. euxenite-(Y) | G4 rim euxenite-(Y) |
|---|---|---|---|---|---|
| MgO | 0.11 | 0.09 | 0.12 | 0.16 | 0.08 |
| CaO | 0.21 | 0.26 | 0.32 | 0.26 | 0.36 |
| $TiO_2$ | 3.77 | 3.98 | 3.78 | 4.16 | 4.11 |
| $Sc_2O_3$ | 0.36 | 0.66 | 0.79 | 0.89 | 1.37 |
| MnO | 1.31 | 1.11 | 1.16 | 1.19 | 1.48 |
| FeO | 8.90 | 9.03 | 8.25 | 8.27 | 7.64 |
| $Y_2O_3$ | 6.74 | 8.58 | 9.89 | 9.97 | 10.12 |
| $Nb_2O_5$ | 37.30 | 34.97 | 37.45 | 36.16 | 34.94 |
| $SnO_2$ | 1.34 | 1.06 | 1.30 | 1.24 | 1.99 |
| $Ta_2O_5$ | 10.50 | 14.01 | 14.02 | 14.03 | 16.79 |
| $WO_3$ | 0.70 | 1.80 | 1.88 | 1.85 | 1.75 |
| $Nd_2O_3$ | 1.18 | 1.12 | 1.32 | 1.15 | 1.31 |
| $Sm_2O_3$ | 0.84 | 0.67 | 0.51 | 0.55 | 0.59 |
| $Gd_2O_3$ | 1.34 | 1.13 | 1.10 | 1.14 | 1.12 |
| $Dy_2O_3$ | 1.28 | 0.89 | 0.45 | 0.57 | 0.62 |
| $Yb_2O_3$ | 0.56 | 1.01 | 0.82 | 0.92 | 0.58 |
| $ThO_2$ | 1.75 | 1.59 | 1.60 | 1.65 | 1.55 |
| $UO_2$ | 20.82 | 15.87 | 11.65 | 11.74 | 10.82 |
| Total | 99.01 | 97.83 | 96.41 | 95.90 | 97.22 |
| | | | | | |
| Mg | 0.012 | 0.010 | 0.013 | 0.017 | 0.010 |
| Ca | 0.016 | 0.020 | 0.024 | 0.020 | 0.020 |
| Ti | 0.202 | 0.214 | 0.201 | 0.221 | 0.216 |
| Sc | 0.022 | 0.041 | 0.048 | 0.055 | 0.084 |
| Mn | 0.079 | 0.067 | 0.069 | 0.071 | 0.088 |
| Fe | 0.531 | 0.539 | 0.485 | 0.489 | 0.447 |
| Y | 0.256 | 0.326 | 0.370 | 0.375 | 0.377 |
| Nb | 1.204 | 1.128 | 1.190 | 1.157 | 1.106 |
| Sn | 0.038 | 0.030 | 0.036 | 0.035 | 0.056 |
| Ta | 0.204 | 0.272 | 0.268 | 0.270 | 0.320 |
| W | 0.013 | 0.033 | 0.034 | 0.034 | 0.032 |
| Nd | 0.030 | 0.029 | 0.033 | 0.029 | 0.033 |
| Sm | 0.021 | 0.016 | 0.012 | 0.013 | 0.014 |
| Gd | 0.032 | 0.027 | 0.026 | 0.027 | 0.026 |
| Dy | 0.029 | 0.020 | 0.010 | 0.013 | 0.014 |
| Yb | 0.012 | 0.022 | 0.018 | 0.020 | 0.012 |
| Th | 0.028 | 0.026 | 0.026 | 0.027 | 0.025 |
| U | 0.331 | 0.252 | 0.182 | 0.185 | 0.169 |
| **Cation Sum** | 3.060 | 3.072 | 3.045 | 3.058 | 3.049 |
| Y+REE | 0.380 | 0.440 | 0.469 | 0.477 | 0.476 |
| Nb+Ta+Ti+W | 1.623 | 1.647 | 1.693 | 1.682 | 1.674 |
| Mn/(Mn+Fe) | 0.129 | 0.110 | 0.124 | 0.127 | 0.164 |
| Ta/(Ta+Nb) | 0.145 | 0.194 | 0.184 | 0.183 | 0.224 |

Structural formula based on 6 oxygen atoms.

prismatic crystals up to 1.6 cm in length (Fig. 7c). The wodginite shows Ta/(Ta + Nb) and Mn/(Mn + Fe) in the ranges of 0.92–0.94 and 0.68–0.70 *apfu*, respectively. It contains $WO_3$ (up to 0.95 wt.%), $UO_2$ (up to 0.11 wt.%), $Gd_2O_3$ (up to 0.07 wt.%), and $Yb_2O_3$ (up to 0.08 wt.%). The unit-cell parameters of wodginite obtained from single-crystal data correspond to a monoclinic cell with *a* 9.532(4), *b* 11.449(4), *c* 5.106(4) Å, ß 90.99(2)°, which agrees well with the wodginite cell reported by Ercit *et al*. (1992).

*Phosphate minerals*. Fluorine-rich triplite [$Mn_2(PO_4)$ F] from the CODp dike occurs within granular albite ± quartz at the pegmatite border as centimetric black masses associated with fluorapatite and Mn-hydroxide minerals. The triplite is fractured with cracks filled with Mn-oxide minerals. The same portion of the pegmatite

TABLE 3. MICROPROBE COMPOSITIONS OF WODGINITE FROM THE VLGb DIKE (LEGGIA VALLEY, BODENGO AREA)

| Oxide (wt.%) | G8 core | G8 rim |
|---|---|---|
| MgO | 0.00 | 0.00 |
| CaO | 0.00 | 0.00 |
| $TiO_2$ | 0.59 | 0.49 |
| $Sc_2O_3$ | 0.00 | 0.00 |
| MnO | 8.41 | 8.39 |
| FeO | 3.95 | 3.62 |
| $Y_2O_3$ | 0.00 | 0.00 |
| $Nb_2O_5$ | 3.36 | 2.72 |
| $SnO_2$ | 14.06 | 14.99 |
| $Ta_2O_5$ | 68.04 | 68.95 |
| $WO_3$ | 0.72 | 0.95 |
| $Gd_2O_3$ | 0.07 | 0.05 |
| $Tb_2O_3$ | 0.00 | 0.00 |
| $Dy_2O_3$ | 0.00 | 0.00 |
| $Er_2O_3$ | 0.00 | 0.00 |
| $Yb_2O_3$ | 0.08 | 0.06 |
| $ThO_2$ | 0.00 | 0.00 |
| $UO_2$ | 0.11 | 0.10 |
| Total | 99.39 | 100.32 |
| | | |
| Mg | 0.000 | 0.000 |
| Ca | 0.000 | 0.000 |
| Ti | 0.048 | 0.040 |
| Sc | 0.000 | 0.000 |
| Mn | 0.778 | 0.772 |
| Fe | 0.361 | 0.329 |
| Y | 0.000 | 0.000 |
| Nb | 0.166 | 0.134 |
| Sn | 0.612 | 0.650 |
| Ta | 2.021 | 2.038 |
| W | 0.020 | 0.027 |
| Gd | 0.003 | 0.002 |
| Tb | 0.000 | 0.000 |
| Dy | 0.000 | 0.000 |
| Er | 0.000 | 0.000 |
| Yb | 0.003 | 0.002 |
| Th | 0.000 | 0.000 |
| U | 0.003 | 0.002 |
| | | |
| **Cation Sum** | 4.015 | 3.994 |
| Y+REE | 0.006 | 0.004 |
| Mn/(Mn+Fe) | 0.683 | 0.701 |
| Ta/(Ta+Nb) | 0.924 | 0.938 |

Structural formula based on 8 oxygen atoms.

contains green-yellow Mn-rich elbaite rimming black Mn-rich schorl tourmaline and colorless to pale pink prismatic beryl. Manganese-rich elbaite has also been reported in pegmatites from Mount Begbie, British Columbia, by Dixon *et al.* (this volume). The triplite plots close to the $Mn_2(PO_4)F$ endmember (Vignola *et al.*, this volume).

Manganese-rich graftonite, $(Ca,Mn)(Fe,Mn)_2(PO_4)_2$, ferrisicklerite, $Li_{1-x}(Fe^{3+},Mn^{2+})PO_4$, Mn-rich apatite, $(Ca,Mn^{2+},Fe^{2+},Mg)(PO_4)_3Cl$, staněkite, $Fe^{3+}Mn^{2+}O(PO_4)$ and Mn-rich vivianite, $(Fe^{2+})_3(PO_4)_2 8H_2O$ occur in a granitic pegmatite from the Bodengo area, together with Be-silicate and Nb-Ta oxide minerals (Guastoni & Grammatica 2001, Guastoni *et al.* 2007).

*Tourmaline*. Tourmaline was analyzed from two dikes of the Codera area (CODp and ROS), from three dikes of the Bodengo area (VDD, VLGa, VLGb), and from the country rock of the pegmatites (PP). The mean compositions are reported in Tables 4 and 5, and plotted in Figure 10. In most cases the composition was measured along profiles from core to rim. The analyzed tourmalines are prismatic black tourmaline (schorl), black graphic tourmaline (CODp2), and yellow-green tourmaline (elbaite). Elbaite was found only in dike CODp1. In the Bodengo area, the most homogeneous tourmaline is from the miarolitic VLGb dike hosted in a leucocratic gneiss; the tourmaline does not show any zoning and is characterized by the lowest Mg number [$Mg/(Mg + Fe2^+) < 0.1$]. The composition of a tourmaline grown in the host rock gneiss of a pegmatite (sample PP) is identical to that of tourmaline from the VLGb sample. The tourmaline from the miarolitic dike VDD is a schorl with a composition very similar to that of VLGb tourmaline (Mg number is slightly higher than 0.1) except for a very tiny (60 μm) rim showing an evolution to higher Mg (as high as 0.25). The schorl tourmaline of VLGa is zoned (Fig. 10d): the core has a foitite composition (vacant *X* site > 0.5) and Mg number of 0.21, which first changes to a lower Mg number and then increase at the rim to as much as 0.35. These outer rims are not foititic in composition. It is of note that both VLGa and VDD dikes intrude amphibolites, which may explain the relatively higher Mg number of the tourmaline. In the Codera area the dominant tourmalines have a similar composition to those in the Bodengo area, but locally show a higher degree of evolution (in the CODp dike). Most of tourmalines, both the prismatic and the graphic types, are schorl. The ROS tourmaline shows a slight zoning with the outer thin rim with a higher Mg number. However, the Codera CODp1 sample also contains yellow-green crystals of Mn-rich elbaite (Ertl *et al.* 2003) and the graphic tourmaline from CODp2 shows thin rims evolving towards elbaite (with similar Mg number as the schorl core). Elbaitic compositions have been found in the Codera area and not in the miarolitic pegmatites of the Bodengo area.

*Garnet*. Garnet was analyzed from three dikes (CODp, CODg, and ROS) in the Codera area and five dikes (VLGa, VLGm, VDD, VG1, and VG2) in the Bodengo area. Selected garnets were embedded in epoxy and polished to expose the crystal core. Microprobe traverses were carried out, rim to rim or core to rim, across each garnet with measuring steps of 50 to 200 μm, depending on the crystal size and zoning. Representative core and rim compositions are reported in Tables 6 and 7. Spessartine (Sps) *versus* almandine (Alm) variation is shown in Figure 11. Core to rim

TABLE 4. TOURMALINE FROM THE CODERA AREA

| Oxide (wt.%) | ROSS pr schorl | # 45 st.dev. | CODp2 pr schorl | # 60 st.dev. | CODp2 graph schorl | # 65 st.dev. | CODp1 pr rim elbaite | # 4 st.dev. | CODp1 pr core schorl | # 4 st.dev. |
|---|---|---|---|---|---|---|---|---|---|---|
| $SiO_2$ | 35.76 | *0.20* | 35.76 | *0.23* | 35.26 | *0.24* | 33.96 | *0.78* | 32.68 | *0.47* |
| $TiO_2$ | 0.13 | *0.03* | 0.16 | 0.05 | 0.21 | *0.04* | 0.22 | *0.06* | 0.18 | *0.07* |
| $Al_2O_3$ | 33.65 | *0.28* | 33.22 | *0.71* | 33.80 | *0.65* | 39.88 | *1.13* | 38.61 | *0.48* |
| FeO | 13.54 | *0.22* | 13.12 | *0.69* | 13.16 | *0.30* | 1.95 | *0.35* | 6.42 | *0.35* |
| MgO | 1.59 | *0.11* | 2.09 | *0.16* | 1.28 | *0.53* | 0.13 | *0.07* | 0.20 | *0.02* |
| CaO | 0.07 | *0.02* | 0.09 | *0.03* | 0.09 | *0.03* | 0.07 | *0.07* | 0.10 | *0.04* |
| MnO | 0.49 | *0.05* | 0.59 | *0.11* | 0.95 | *0.20* | 4.75 | *0.26* | 3.49 | *0.23* |
| ZnO | 0.32 | *0.04* | 0.32 | *0.06* | 0.43 | *0.13* | 0.00 | *0.00* | 0.00 | *0.00* |
| $Na_2O$ | 1.96 | *0.12* | 2.04 | *0.12* | 2.02 | *0.13* | 2.52 | *0.29* | 2.05 | *0.11* |
| $K_2O$ | 0.04 | *0.01* | 0.05 | *0.01* | 0.05 | *0.01* | 0.00 | *0.00* | 0.00 | *0.00* |
| F | 0.33 | *0.15* | 0.28 | *0.15* | 0.40 | *0.18* | 1.20 | *0.27* | 0.69 | 0.06 |
| $H_2O$* | 3.47 | | 3.48 | | 3.41 | | 3.09 | | 3.24 | |
| $B_2O_3$* | 10.49 | | 10.48 | | 10.44 | | 10.59 | | 10.34 | |
| $Li_2O$* | 0.17 | | 0.15 | | 0.19 | | 1.11 | | 0.57 | |
| Total | 101.87 | | 101.72 | | 101.54 | | 98.96 | | 98.27 | |
| | | | | | | | | | | |
| Si | 5.923 | | 5.931 | | 5.872 | | 5.572 | | 5.494 | |
| Al | 0.077 | | 0.070 | | 0.128 | | 0.428 | | 0.506 | |
| **Sum T site** | 6.000 | | 6.001 | | 6.000 | | 6.000 | | 6.000 | |
| Al | 6.000 | | 6.000 | | 6.000 | | 6.000 | | 6.000 | |
| Mg | 0.000 | | 0.000 | | 0.000 | | 0.000 | | 0.000 | |
| $Fe^{3+}$ | 0.000 | | 0.000 | | 0.000 | | 0.000 | | 0.000 | |
| **Sum Z site** | 6.000 | | 6.000 | | 6.000 | | 6.000 | | 6.000 | |
| Al | 0.493 | | 0.423 | | 0.506 | | 1.282 | | 1.143 | |
| Ti | 0.016 | | 0.020 | | 0.027 | | 0.027 | | 0.023 | |
| $Fe^{3+}$ | 0.000 | | 0.000 | | 0.000 | | 0.000 | | 0.000 | |
| Mg | 0.392 | | 0.516 | | 0.318 | | 0.031 | | 0.050 | |
| Mn | 0.069 | | 0.083 | | 0.134 | | 0.660 | | 0.496 | |
| $Fe^{2+}$ | 1.875 | | 1.820 | | 1.833 | | 0.267 | | 0.902 | |
| Zn | 0.039 | | 0.040 | | 0.053 | | 0.000 | | 0.000 | |
| Li* | 0.115 | | 0.098 | | 0.129 | | 0.733 | | 0.385 | |
| **Sum Y site** | 3.000 | | 3.000 | | 3.000 | | 3.000 | | 3.000 | |
| Ca | 0.012 | | 0.016 | | 0.016 | | 0.012 | | 0.018 | |
| Na | 0.631 | | 0.657 | | 0.654 | | 0.801 | | 0.668 | |
| K | 0.008 | | 0.011 | | 0.011 | | 0.000 | | 0.000 | |
| □ | 0.348 | | 0.317 | | 0.320 | | 0.187 | | 0.315 | |
| **Sum X site** | 1.000 | | 1.000 | | 1.000 | | 1.000 | | 1.000 | |
| B | 3.000 | | 3.000 | | 3.000 | | 3.000 | | 3.000 | |
| OH | 3.829 | | 3.851 | | 3.789 | | 3.378 | | 3.636 | |
| F | 0.171 | | 0.149 | | 0.211 | | 0.622 | | 0.364 | |
| **Sum W site** | 4.000 | | 4.000 | | 4.000 | | 4.000 | | 4.000 | |
| $Mg/(Mg+Fe^{2+})$ | 0.17 | | 0.22 | | 0.15 | | 0.10 | | 0.05 | |
| $2Li/(2Li+Mg+Fe^{2+})$ | 0.09 | | 0.08 | | 0.11 | | 0.83 | | 0.45 | |

Structural formula based on 31 anions (O, OH, F), calculated using the program by Julie Selway (Ontario Geological Survey).

spessartine zoning profiles of representative garnets are plotted in Figure 12.

Garnet from the CODp (phosphate-bearing) and CODg dikes is dark-red, sub-euhedral, and often surrounded by aggregates of graphic garnet intergrown with feldspar and quartz. Euhedral and graphic garnet from the CODp samples is fairly homogeneous, ranging from $Alm_{32}Sps_{64}Pyr_2$ (core) to $Alm_{36}Sps_{61}Pyr_2$ (rim); the sum of grossularia, andradite, and uvarovite components is always less than 5 mol.%. A distinctive spessartine-rich ($Alm_{7-17}Sps_{92-82}Pyr_{05-0.3}$) garnet is also found in the CODp dike. Garnet from the CODg dike shows a moderate zoning with a core composition similar to that of CODp cores, and rim composition enriched in the almandine component ($Alm_{44}Sps_{53}Pyr_2$). Garnet from the ROS dike shows a homogeneous core ($Alm_{31}Sps_{64}Pyr_3$), almost overlapping CODp and CODg compositions (Fig. 12), and a rim showing a

progressive zoning towards an almandine-rich composition ($Alm_{53}Sps_{39}Pyr_6$).

Garnet from the Bodengo area (VLGa, VDD, VG1, VG2, PP) is typically dark red in color and mostly shows deltoidal icositetrahedron habit. Garnet from the VLGa, VDD, and VG2 dikes shows a bell-shaped profile (Fig. 12), with a compositionally homogeneous core ($Alm_{57}Sps_{41}Pyr_{0.7}$) and a rim showing a sharp increase in almandine (and decrease in spessartine) component up to $Alm_{73}Sps_{23}Pyr_3$. Garnet from the VG2 dike shows the highest spessartine core content ($Alm_{46}Sps_{48}Pyr_4$) of the Bodengo samples. Garnet from the VLGm monazite-bearing dike of the Val Leggia valley is black and shows a rhomb-dodecahedron habit. The composition of the VLGm garnet (core $Alm_{29}Sps_{65}Py_4$ to rim $Alm_{40}Sps_{51}Py_5$) is remarkably different from those typical of the Bodengo area and almost overlaps those from the Codera area (Fig. 12), but shows a distinctive higher $TiO_2$ content. Except for this sample, the compositions of garnets from the

TABLE 5. TOURMALINE FROM THE BODENGO AREA

| Oxide (wt.%) | VLG a Pr core foitite | # 40 *st.dev.* | VLG a Pr int schorl | # 61 *st.dev.* | VLG a Pr rim schorl | # 18 *st.dev.* | VLG b pr schorl | # 68 *st.dev.* | VDD pr schorl | # 59 *st.dev.* | PP bulk schorl |
|---|---|---|---|---|---|---|---|---|---|---|---|
| $SiO_2$ | 36.26 | *0.35* | 35.84 | *0.31* | 35.80 | *0.40* | 35.01 | *0.23* | 35.34 | *0.32* | 35.62 |
| $TiO_2$ | 0.17 | *0.11* | 0.37 | *0.10* | 0.67 | *0.06* | 0.50 | *0.03* | 0.14 | *0.11* | 0.11 |
| $Al_2O_3$ | 35.09 | *0.32* | 34.56 | *0.33* | 33.95 | *0.35* | 34.28 | *0.18* | 34.16 | *0.41* | 34.34 |
| FeO | 12.13 | *0.56* | 12.67 | *0.58* | 11.34 | *0.65* | 14.18 | *0.24* | 13.97 | *0.23* | 14.3 |
| MgO | 1.84 | *0.30* | 1.66 | *0.38* | 2.85 | *0.19* | 0.40 | *0.09* | 0.96 | *0.16* | 0.44 |
| CaO | 0.07 | *0.02* | 0.08 | *0.04* | 0.14 | *0.03* | 0.02 | *0.01* | 0.06 | *0.02* | 0.11 |
| MnO | 0.22 | *0.03* | 0.21 | *0.04* | 0.09 | *0.03* | 0.24 | *0.03* | 0.23 | *0.03* | 0.15 |
| ZnO | 0.09 | *0.04* | 0.13 | *0.05* | 0.09 | *0.03* | 0.62 | *0.10* | 0.12 | *0.04* | n.a. |
| $Na_2O$ | 1.42 | *0.06* | 1.74 | *0.10* | 1.93 | *0.05* | 2.19 | *0.06* | 1.82 | *0.17* | 1.83 |
| $K_2O$ | 0.03 | *0.01* | 0.04 | *0.01* | 0.04 | *0.01* | 0.04 | *0.01* | 0.04 | *0.01* | n.a. |
| F | 0.09 | *0.10* | 0.15 | *0.10* | 0.24 | *0.10* | 0.94 | *0.16* | 0.33 | *0.16* | n.a. |
| $H_2O$* | 3.62 | | 3.58 | | 3.54 | | 3.16 | | 3.44 | | 3.61 |
| $B_2O_3$* | 10.63 | | 10.57 | | 10.58 | | 10.45 | | 10.43 | | 10.46 |
| $Li_2O$* | 0.22 | | 0.25 | | 0.27 | | 0.32 | | 0.22 | | 0.33 |
| Total | 101.85 | | 101.79 | | 101.45 | | 101.95 | | 101.12 | | 101.30 |
| | | | | | | | | | | | |
| Si | 5.928 | | 5.893 | | 5.882 | | 5.823 | | 5.891 | | 5.920 |
| Al | 0.072 | | 0.107 | | 0.118 | | 0.177 | | 0.109 | | 0.080 |
| **Sum T site** | 6.000 | | 6.000 | | 6.000 | | 6.000 | | 6.000 | | 6.000 |
| Al | 6.000 | | 6.000 | | 6.000 | | 6.000 | | 6.000 | | 6.000 |
| Mg | 0.000 | | 0.000 | | 0.000 | | 0.000 | | 0.000 | | 0.000 |
| $Fe^{3+}$ | 0.000 | | 0.000 | | 0.000 | | 0.000 | | 0.000 | | 0.000 |
| **Sum Z site** | 6.000 | | 6.000 | | 6.000 | | 6.000 | | 6.000 | | 6.000 |
| Al | 0.689 | | 0.590 | | 0.455 | | 0.542 | | 0.602 | | 0.646 |
| Ti | 0.021 | | 0.046 | | 0.083 | | 0.062 | | 0.018 | | 0.014 |
| $Fe^{3+}$ | 0.000 | | 0.000 | | 0.000 | | 0.000 | | 0.000 | | 0.000 |
| Mg | 0.448 | | 0.407 | | 0.699 | | 0.099 | | 0.238 | | 0.109 |
| Mn | 0.030 | | 0.029 | | 0.012 | | 0.034 | | 0.033 | | 0.021 |
| $Fe^{2+}$ | 1.659 | | 1.743 | | 1.559 | | 1.972 | | 1.947 | | 1.988 |
| Zn | 0.011 | | 0.015 | | 0.011 | | 0.076 | | 0.015 | | 0.000 |
| Li* | 0.142 | | 0.168 | | 0.181 | | 0.213 | | 0.147 | | 0.222 |
| **Sum Y site** | 3.000 | | 3.000 | | 3.002 | | 3.000 | | 3.000 | | 3.000 |
| Ca | 0.012 | | 0.014 | | 0.025 | | 0.003 | | 0.011 | | 0.020 |
| Na | 0.452 | | 0.553 | | 0.615 | | 0.707 | | 0.587 | | 0.590 |
| K | 0.007 | | 0.009 | | 0.009 | | 0.009 | | 0.008 | | 0.000 |
| □ | 0.529 | | 0.423 | | 0.352 | | 0.282 | | 0.394 | | 0.391 |
| **Sum X site** | 1.000 | | 1.000 | | 1.000 | | 1.000 | | 1.000 | | 1.000 |
| B | 3.000 | | 3.000 | | 3.000 | | 3.000 | | 3.000 | | 3.000 |
| OH | 3.951 | | 3.922 | | 3.877 | | 3.507 | | 3.826 | | 4.000 |
| F | 0.049 | | 0.078 | | 0.123 | | 0.493 | | 0.174 | | 0.000 |
| **Sum W site** | 4.000 | | 4.000 | | 4.000 | | 4.000 | | 4.000 | | 4.00 |
| $Mg/(Mg+Fe^{2+})$ | 0.21 | | 0.19 | | 0.31 | | 0.05 | | 0.11 | | 0.05 |
| $2Li/(2Li+Mg+Fe^{2+})$ | 0.12 | | 0.14 | | 0.14 | | 0.17 | | 0.12 | | 0.18 |

Structural formula based on 31 anions (O, OH, F), calculated using the program by Julie Selway (Ontario Geological Survey). The square symbol indicates a vacancy.

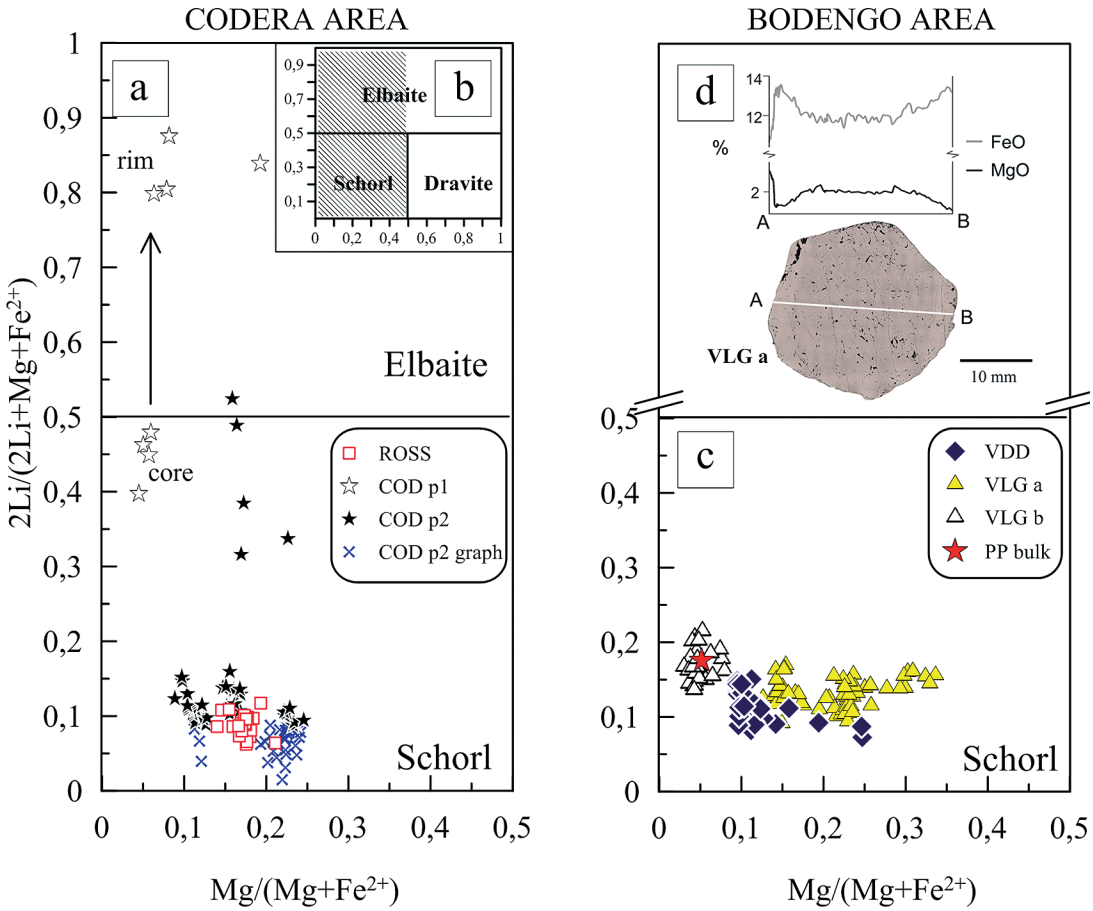


FIG. 10. Classification diagram of tourmaline from the Codera (a) and the Bodengo (c) areas. The complete classification scheme is reported in the inset (b). The compositional profile of a zoned tourmaline crystal from the VLGa dike is shown in (d).

Bodengo area are significantly different from those of the Codera area, showing lower MnO and higher FeO contents. Zoned garnets from both areas show similar zoning pattern of MnO depletion and FeO enrichment from core to rim (Tables 6 and 7).

## GEOCHEMISTRY OF PEGMATITES

Granitic pegmatites of the rare-element and miarolitic classes (Černý & Ercit 2005) display the strongest fractionation and enrichment of (1) LILE (large-ion lithophile elements) such as K, Rb, Sr, Cs, and Ba, (2) HFSE (high field strength elements) such as Zr, Hf, Nb, Ta, REE, U, Th, and (3) light elements, volatiles, and semi-volatiles such as Li, Be, B, F, and P (London 1992). The enrichment of these incompatible trace elements is reflected in the occurrence of some specific minerals (*e.g.*, columbite, beryl, tourmaline, and REE minerals). The bulk chemical composition of the pegmatite is difficult to quantify reliably, as it is commonly hindered by the heterogeneous, zoned texture of the dikes and by the large crystal size (as much as meters). However, trace element contents in single mineral phases or in fine-grained portions of the dike can provide useful information, which helps to constrain the pegmatite evolution and support the mineral-based classification (Černý 1991a, Černý 1991b, London 2008).

Bulk rock and trace-element analysis of dikes from Codera and Bodengo areas were performed by Inductively Coupled Plasma-Optical Emission Spectrometry (ICP-OES) and Inductively Coupled Plasma-Mass Spectrometry (ICP-MS). Details on the analytical technique can be found in the Appendix. Selected bulk trace-element contents of some fine-grained portions of pegmatites and of single mineral phases (K-feldspar,

micas, tourmaline, and beryl) from both the Codera and Bodengo areas are reported in Table 8. The complete major and trace element analyses are reported in Table SOM1 (available from the Depository of Unpublished Data on the MAC website, document CM52_191). The most evolved geochemical signature is observed for the CODp and VLGb dikes. In CODp (1) the graphic texture of the intermediate zone contains 947 ppm Cs and 1594 ppm Rb; (2) muscovite + biotite contains 1093 ppm Rb and 169 ppm Ga. In the VLGb dike the minerals from the miarolitic cavities contain (1) 1492 ppm Cs, 3498 ppm Rb, and 189 ppm Ga in muscovite; (2) 671 ppm Cs and 2433 ppm Rb in microcline; (3) 579 ppm Cs in beryl (*versus* 542 ppm Cs in beryl from the border zone of the dike).

Other dikes from the same areas show remarkably different trace element compositions of minerals. Sample VLGa, with a giant crystal size in the dike core, contains (1) 4 ppm Cs and 497 ppm Rb in microcline (large crystals from the dike core); and (2) 167 ppm Cs and 30 ppm Rb in beryl. Sample CODg contains (1) 16 ppm Cs and 818 ppm Rb in perthitic K-feldspar from the core zone; (2) 19 ppm Cs and 485 ppm Rb in microcline in graphic intergrowth with quartz; and (3) 144 ppm Cs, 1583 ppm Rb, and 111 ppm Ga in biotite.

The bulk chemistry of garnet-muscovite-bearing aplite from the Bodengo area, which is the dominant type in the pegmatite field, has been analyzed for comparison. In contrast with the evolved dikes, this sample does not show any significant enrichment in Cs (1 ppm), Rb (48 ppm), or Ga (20 ppm).

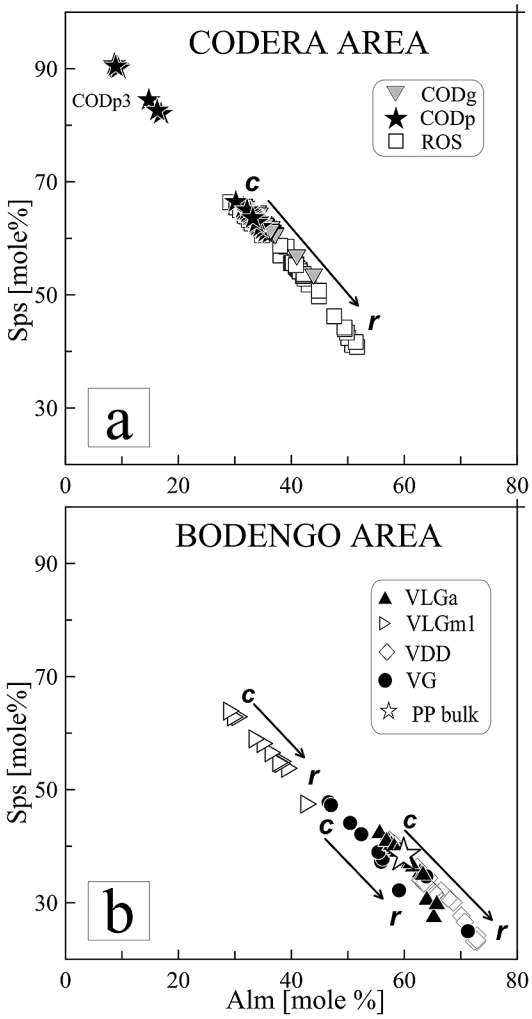


FIG. 11. Almandine (Alm) *versus* spessartine (Sps) component plot illustrating the composition of garnet from the Codera and Bodengo areas. Garnet from the Codera area is predominantly spessartine (Sps>50%), with minor almandine rims. The highest spessartine content (80–90%) is from garnet of the phosphate-bearing dike of the Codera area (CODp). Garnet from the Bodengo area is typically almandine (Alm>50 %), with the only exception being garnet from the monazite-bearing dike of the Leggia Valley (VLGm), whose composition overlaps garnet from the Codera area. Arrows indicate core (c) to rim (r) compositional trends.

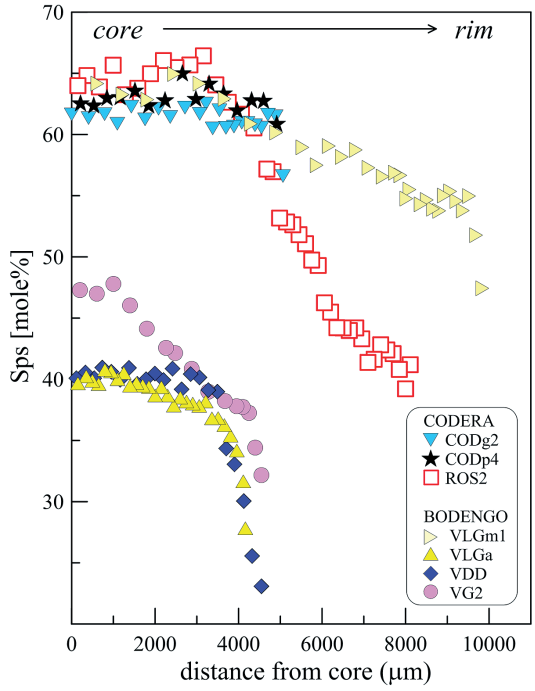


FIG. 12. Zoning patterns of spessartine content (Sps mole%) in selected garnets from the Codera and Bodengo areas.

TABLE 6. GARNET FROM THE CODERA AREA

| Oxide (wt.%) | CODp3 core | CODp3 rim | CODp4 core | CODp4 rim | CODp4g core | CODp4g rim | CODg core | CODg rim | ROS2 core | ROS2 rim |
|---|---|---|---|---|---|---|---|---|---|---|
| $SiO_2$ | 35.90 | 35.61 | 35.34 | 36.14 | 35.57 | 35.98 | 35.77 | 36.18 | 35.14 | 36.38 |
| $TiO_2$ | 0.02 | 0.08 | 0.11 | 0.05 | 0.09 | 0.06 | 0.09 | 0.05 | 0.12 | 0.05 |
| $Al_2O_3$ | 20.82 | 20.32 | 19.96 | 20.08 | 20.02 | 19.94 | 20.27 | 20.28 | 19.79 | 20.42 |
| $Cr_2O_3$ | 0.01 | 0.00 | 0.00 | 0.01 | 0.01 | 0.01 | 0.02 | 0.02 | 0.01 | 0.02 |
| FeO* | 3.06 | 7.23 | 13.45 | 15.50 | 13.40 | 15.04 | 13.52 | 19.03 | 12.64 | 22.92 |
| $Fe_2O_3$* | 0.53 | 0.62 | 2.54 | 0.50 | 2.00 | 0.69 | 1.26 | 0.41 | 2.36 | 0.55 |
| MnO | 39.11 | 34.55 | 27.06 | 26.05 | 27.55 | 26.29 | 27.67 | 22.77 | 27.32 | 16.91 |
| MgO | 0.02 | 0.06 | 0.55 | 0.48 | 0.45 | 0.49 | 0.44 | 0.51 | 0.66 | 1.48 |
| CaO | 0.19 | 0.25 | 0.40 | 0.41 | 0.39 | 0.42 | 0.41 | 0.24 | 0.50 | 0.67 |
| Total | 99.66 | 98.73 | 99.42 | 99.21 | 99.48 | 98.91 | 99.45 | 99.49 | 98.54 | 99.39 |
| | | | | | | | | | | |
| Si | 2.968 | 2.975 | 2.936 | 2.999 | 2.952 | 2.996 | 2.965 | 2.995 | 2.941 | 2.991 |
| Ti | 0.002 | 0.005 | 0.007 | 0.003 | 0.006 | 0.004 | 0.005 | 0.003 | 0.008 | 0.003 |
| Al | 2.028 | 2.001 | 1.955 | 1.964 | 1.959 | 1.957 | 1.980 | 1.978 | 1.953 | 1.978 |
| Cr | 0.000 | 0.000 | 0.000 | 0.000 | 0.001 | 0.000 | 0.001 | 0.001 | 0.001 | 0.001 |
| $Fe^{3+}$ | 0.033 | 0.039 | 0.159 | 0.031 | 0.125 | 0.043 | 0.079 | 0.026 | 0.148 | 0.034 |
| $Fe^{2+}$ | 0.212 | 0.505 | 0.935 | 1.076 | 0.930 | 1.047 | 0.937 | 1.317 | 0.884 | 1.576 |
| Mn | 2.739 | 2.445 | 1.905 | 1.831 | 1.937 | 1.854 | 1.943 | 1.596 | 1.937 | 1.177 |
| Mg | 0.002 | 0.008 | 0.068 | 0.059 | 0.056 | 0.061 | 0.054 | 0.063 | 0.083 | 0.182 |
| Ca | 0.017 | 0.022 | 0.036 | 0.036 | 0.035 | 0.038 | 0.036 | 0.021 | 0.045 | 0.059 |
| **Cation Sum** | 8.000 | 8.000 | 8.000 | 8.000 | 8.000 | 8.000 | 8.000 | 8.000 | 8.000 | 8.000 |
| Py | 0.07 | 0.27 | 2.25 | 1.97 | 1.86 | 2.02 | 1.79 | 2.11 | 2.74 | 6.05 |
| Al | 8.15 | 17.64 | 33.39 | 35.77 | 32.65 | 34.91 | 32.42 | 44.00 | 31.49 | 52.78 |
| Sp | 91.22 | 81.35 | 63.17 | 61.05 | 64.33 | 61.81 | 64.58 | 53.19 | 64.29 | 39.22 |
| Uv | 0.02 | 0.00 | 0.00 | 0.02 | 0.04 | 0.02 | 0.06 | 0.06 | 0.04 | 0.06 |
| An | 0.00 | 0.69 | 4.37 | 1.70 | 3.60 | 2.14 | 2.05 | 1.13 | 4.23 | 1.29 |
| Gr | 0.56 | 0.74 | 1.19 | 1.21 | 1.15 | 1.26 | 1.21 | 0.71 | 1.49 | 1.95 |

Structural formula based on 12 oxygen atoms. * ($Fe^{3+}/Fe^{2+}$) calculated (Droop 1987).

## Pegmatite Classification

We attempted to classify the pegmatite dikes for which we have chemical compositions (with the exception of the VLGm dike), using the classification scheme of Černý (1982, 1991a) and Černý & Ercit (2005). This classification integrates different data sets including the pressure-temperature conditions of the host rock and the pegmatite mineral assemblage, chemistry, and texture. The pegmatite dikes considered for classification plot in the LCT and mixed NYF-LCT families with the exception of the monazite-bearing VLGm dike, which is classified as a NYF pegmatite. While the pegmatite subclass and type can be defined according to the scheme of Černý & Ercit (2005), a new "beryl pegmatite subtype" has been introduced (Table 9).

## Discussion

### *Pressure-temperature conditions of the host rocks during pegmatite intrusion*

In the Codera valley, the maximum pressure-temperature conditions of the host rock during the emplacement of pegmatites are constrained by the intrusion depth of the Bergell batholith and the metamorphic conditions of migmatization coeval with the pluton emplacement. The Bergell intrusion depth was estimated at about 22–26 km on the basis of Al-in-hornblende barometry, which yielded 0.62 ± 0.05 GPa for samples close to Bivacco Marinetti in the upper Codera valley (Davidson *et al*. 1996, Reusser 1987), which is the same COD locality where most our pegmatite and mylonite samples come from. Migmatization in the Gruf complex host rocks was coeval with the emplacement of the Bergell batholith and was estimated by Galli (2013) to occur at 0.6–0.7 GPa and 700–750 °C (to as much as 750–755 °C close to the pluton contact). These ambient conditions clearly exceeded the conditions of pegmatite intrusion. The pegmatites crosscut (1) the intrusive contact between the Bergell pluton and the Gruf complex, (2) the pervasive solid-state foliation of the intrusive rocks developed parallel to the contact, and (3) the main fabric of the Gruf migmatites. However, pegmatites were involved in localized ductile deformation. In two of the analyzed quartz mylonites (from such ductilely deformed pegmatites) the measured crystallographic preferred orientation shows a strong, single *c*-axis maximum parallel to the Y-axis of the mylonite (*i.e*., orthogonal to lineation and in the foliation plane).

This quartz CPO pattern has been recognized to occur at relatively high temperature in deformed quartz veins sheared within the metamorphic contact aureole of the Tertiary Adamello batholith (Stipp *et al*. 2002). The temperature of deformation of the Adamello quartz veins, and of the corresponding microstructure and CPO, was determined from the mineral assemblage of the host synkinematic micaschist mylonites. The appearance of the single Y-maximum of the *c*-axis was observed to occur abruptly with increasing temperature across the sheared metamorphic contact aureole, at ~500 °C (Stipp *et al*. 2002). This approximate temperature is consistent with the mineral assemblage and microstructures of the Bergell tonalite mylonites, associated with the quartz mylonites, that include recrystallization of quartz, biotite, and feldspar. The CPO of the Bergell quartz mylonites is directly comparable with that determined for the quartz mylonites within the Adamello batholith (the largest batholith of the Oligocene Alpine intrusions along the Periadriatic Fault; Fig. 1a), which are also associated with mylonites having stable biotite and feldspar (oligoclase and K-feldspar) in the foliation (Pennacchioni 2005, Pennacchioni *et al*. 2010). Similar mylonites developed under high-grade conditions were observed to occur in other plutons during post-magmatic cooling (*e.g*., Pennacchioni & Zucchi 2013), including the Novate intrusion (Ciancaleoni & Marquer 2006). We infer that intrusion of pegmatites and their deformation in the Codera area was at a host rock temperature of about 500 °C. The pressure conditions of pegmatite intrusion and deformation are less constrained. It can be reasonably assumed that rapid cooling of the Bergell batholith (Hansmann 1996) and of its host rocks from synmagmatic conditions (*ca*. 750 °C at 0.6 GPa) was likely associated with rapid exhumation of the Bergell batholith related to backfolding and backthrusting of the Alpine nappe stack against the Periadriatic Fault. Therefore, the pegmatites intruded the Gruf complex and the Bergell intrusive rocks after they had been partially exhumed, but were still hot.

In the Bodengo area, the metamorphic conditions during the D3 phase (650–750 °C and 0.4–0.6 GPa; Nagel *et al*. 2002) can be assumed to be the upper limit of pressure-temperature conditions for the emplacement of pegmatites. These conditions are similar to those of the Codera area and similarly exceed the conditions of intrusion of the pegmatites. The pegmatites of the main set of the Bodengo area are mostly undeformed and crosscut the folds of the D3 phase, indicating that they postdated the main ductile deformation in the

TABLE 7. GARNET FROM THE BODENGO AREA

| Oxide (wt.%) | VLGa core | VLGa rim | VLGm core | VLGm rim | VDD3 core | VDD3 rim | VG1 core | VG1 rim | VG2 core | VG2 rim | PP bulk |
|---|---|---|---|---|---|---|---|---|---|---|---|
| $SiO_2$ | 35.57 | 36.24 | 36.15 | 36.95 | 35.80 | 35.99 | 35.90 | 36.50 | 36.16 | 36.78 | 34.94 |
| $TiO_2$ | 0.07 | 0.02 | 0.35 | 0.14 | 0.05 | 0.02 | 0.05 | 0.01 | 0.11 | 0.01 | 0.06 |
| $Al_2O_3$ | 20.55 | 21.02 | 19.67 | 20.32 | 20.61 | 20.75 | 20.66 | 20.92 | 20.66 | 20.99 | 20.38 |
| $Cr_2O_3$ | 0.01 | 0.00 | 0.01 | 0.01 | 0.00 | 0.01 | 0.01 | 0.04 | 0.01 | 0.02 | 0.20 |
| FeO* | 24.24 | 29.11 | 13.12 | 18.16 | 24.59 | 31.45 | 25.08 | 30.34 | 20.48 | 25.35 | 24.66 |
| $Fe_2O_3$* | 1.26 | 0.52 | 0.00 | 0.00 | 0.83 | 0.79 | 0.03 | 0.00 | 0.35 | 0.00 | 1.14 |
| MnO | 17.41 | 11.54 | 27.25 | 22.05 | 17.40 | 9.75 | 16.94 | 10.81 | 20.14 | 14.01 | 16.22 |
| MgO | 0.27 | 1.10 | 0.96 | 1.33 | 0.18 | 0.70 | 0.20 | 0.66 | 1.00 | 1.72 | 0.29 |
| CaO | 0.19 | 0.47 | 0.80 | 0.90 | 0.26 | 0.37 | 0.30 | 0.37 | 0.53 | 0.62 | 0.18 |
| Total | 99.57 | 100.01 | 98.32 | 99.86 | 99.73 | 99.83 | 99.16 | 99.65 | 99.43 | 99.49 | 97.95 |
| | | | | | | | | | | | |
| Si | 2.951 | 2.968 | 3.013 | 3.019 | 2.965 | 2.966 | 2.984 | 3.001 | 2.979 | 3.003 | 2.942 |
| Ti | 0.004 | 0.001 | 0.022 | 0.009 | 0.003 | 0.001 | 0.003 | 0.000 | 0.007 | 0.000 | 0.004 |
| Al | 2.009 | 2.029 | 1.932 | 1.957 | 2.012 | 2.015 | 2.024 | 2.027 | 2.006 | 2.019 | 2.023 |
| Cr | 0.001 | 0.000 | 0.001 | 0.001 | 0.000 | 0.000 | 0.001 | 0.002 | 0.000 | 0.001 | 0.013 |
| $Fe^{3+}$ | 0.079 | 0.032 | 0.000 | 0.000 | 0.052 | 0.049 | 0.002 | 0.000 | 0.021 | 0.000 | 0.072 |
| $Fe^{2+}$ | 1.682 | 1.994 | 0.915 | 1.241 | 1.703 | 2.168 | 1.743 | 2.087 | 1.411 | 1.731 | 1.737 |
| Mn | 1.223 | 0.800 | 1.924 | 1.526 | 1.221 | 0.681 | 1.193 | 0.753 | 1.405 | 0.969 | 1.157 |
| Mg | 0.033 | 0.134 | 0.120 | 0.162 | 0.022 | 0.086 | 0.024 | 0.081 | 0.123 | 0.209 | 0.036 |
| Ca | 0.017 | 0.041 | 0.072 | 0.078 | 0.023 | 0.033 | 0.026 | 0.033 | 0.047 | 0.055 | 0.016 |
| **Cation Sum** | 8.000 | 8.000 | 7.998 | 7.993 | 8.000 | 8.000 | 8.000 | 7.984 | 8.000 | 7.987 | 8.000 |
| Py | 1.10 | 4.46 | 4.02 | 5.46 | 0.73 | 2.87 | 0.82 | 2.73 | 4.11 | 7.05 | 1.21 |
| Al | 57.72 | 67.50 | 29.04 | 40.53 | 57.94 | 73.40 | 58.39 | 70.66 | 47.56 | 58.41 | 59.87 |
| Sp | 40.61 | 26.67 | 64.54 | 51.36 | 40.57 | 22.63 | 39.90 | 25.50 | 46.79 | 32.71 | 38.38 |
| Uv | 0.04 | 0.00 | 0.03 | 0.04 | 0.02 | 0.02 | 0.03 | 0.12 | 0.02 | 0.05 | 0.67 |
| An | 1.14 | 0.00 | 2.48 | 1.83 | 0.56 | 0.41 | 0.00 | 0.00 | 0.21 | 0.00 | 0.19 |
| Gr | 0.57 | 1.37 | 2.41 | 2.64 | 0.76 | 1.10 | 0.89 | 1.11 | 1.55 | 1.84 | 0.54 |

Structural formula based on 12 oxygen atoms. * ($Fe^{3+}/Fe^{2+}$) calculated (Droop 1987).

TABLE 8. BULK-ROCK AND MINERAL COMPOSITION

| | | Ba | Rb | K/Rb | Ga | Rb/Sr | Sr | Al/Ga | K/Cs | Cs |
|---|---|---|---|---|---|---|---|---|---|---|
| **CODERA AREA** | | | | | | | | | | |
| ***CODg*** | | | | | | | | | | |
| A2 | bulk rock (border zone) | 204 | 173 | 184 | 18 | 1.3 | 131 | 4400 | 4542 | 7 |
| A7 | bt | 27 | 1583 | 47 | 111 | 528 | 3 | 812 | 515 | 144 |
| A1 | mc-qz graphic texture | 12 | 485 | 162 | 17 | 48.5 | 10 | 4379 | 4126 | 19 |
| A3 | perthitic kfs | 15 | 818 | 124 | 30 | 117 | 7 | 3335 | 6320 | 16 |
| ***CODp*** | | | | | | | | | | |
| B2 | bulk rock (aplite apophysis | 822 | 380 | 79 | 24 | 1 | 374 | 4048 | 1251 | 24 |
| B1 | ab+qz (wall zone with elbaite) | 0 | 35 | 81 | 33 | 5.8 | 6 | 2544 | 83 | 34 |
| B5 | ms+bt | 2 | 1093 | 81 | 169 | 1093 | 1 | 1019 | 3162 | 28 |
| B3 | mc-qz graphic texture | 45 | 1594 | 54 | 69 | 177 | 9 | 1417 | 91 | 947 |
| **BODENGO AREA** | | | | | | | | | | |
| ***Bodengo aplite*** | | | | | | | | | | |
| W1 | bulk rock | 48 | 46 | 152 | 44 | 0.3 | 148 | 4010 | 6970 | 1 |
| ***VLGa*** | | | | | | | | | | |
| P1 | schorl (inner zone) | 8 | 1 | 332 | 79 | 0 | 1 | 2561 | 0 | 0 |
| P2 | brl (inner zone) | 0 | 30 | 3 | 15 | 30 | 1 | 6229 | 0.3 | 167 |
| P3 | grt (inner zone) | 2 | 11 | 53 | 49 | 11 | 1 | 2202 | 0 | 0 |
| P6 | giant mc (inner zone) | 4 | 497 | 204 | 15 | 497 | 1 | 6607 | 25405 | 4 |
| ***VLGb*** | | | | | | | | | | |
| R3 | bulk rock (border zone) | 117 | 139 | 193 | 20 | 1.9 | 73 | 3968 | 1490 | 18 |
| R2 | brl (border zone) | 0 | 35 | 24 | 23 | 35 | 1 | 3450 | 1.5 | 542 |
| R1 | kfs (miarolitic cavity) | 3 | 2433 | 43 | 23 | 243 | 10 | 4373 | 156 | 671 |
| R5 | tur (miarolitic cavity) | 2 | 5 | 116 | 85 | 5 | 1 | 2207 | 97 | 6 |
| R6 | brl (miarolitic cavity) | 0 | 34 | 20 | 22 | 34 | 1 | 4777 | 1 | 579 |
| R7 | ms (miarolitic cavity) | 1 | 3498 | 25 | 189 | 3498 | 1 | 1020 | 59 | 1492 |

TABLE 9. CLASSIFICATION OF SELECTED PEGMATITE DIKES

| Pegmatite Dike | Family | Class | Subclass | Type | Subtype | Mineral composition |
|---|---|---|---|---|---|---|
| VLGa | LCT | rare element (REL) | rare element-Li (REL-Li) | beryl | beryl-columbite | K-feldspar, albite, quartz, muscovite, biotite, beryl, schorl, almandine-spessartine ($Sps_{41}Alm_{58}Pyr_1$) zircon |
| CODp | LCT | rare element (REL) | rare element-Li (REL-Li) | beryl | beryl-columbite-phosphate | K-feldspar, albite, quartz, greenish K-feldspar, Rb-rich K-feldspar, muscovite, biotite, colorless to pale pink beryl, spessartine-almandine ($Sps_{64}Alm_{34}Pyr_2$), Mn-rich elbaite, Mn-rich fluor-elbaite, Mn-rich elbaite-schorl, F-rich triplite, Mn-hydroxides, spessartine ($Sps_{92}Alm_8Pyr_0$) |
| VLGb | | miarolitic | rare element-Li (REL-Li) | beryl-topaz | beryl* | K-feldspar, albite, albite var. cleavelandite, quartz, muscovite, beryl, schorl, spessartine-almandine wodginite, zircon |
| CODg | mixed NYF-LCT | rare element (REL) | | | | K-feldspar, albite, quartz, muscovite, biotite, spessartine-almandine ($Sps_{65}Alm_{33}Pyr_2$), beryl, columbite-(Fe), euxenite-(Y), magnetite. monazite-(Ce), xenotime-(Y), uraninite, zircon |
| VLGm | NYF | miarolitic | miarolitic-REE (MI-REE) | | | K-feldspar, albite, quartz, aeschynite-(Y), biotite, columbite-(Fe), euxenite-(Y), monazite-(Ce), spessartine-almandine ($Sps_{65}Alm_{31}Pyr_4$), zircon |
| Bodengo aplite | barren or ceramics | muscovite | | | | K-feldspar, albite, quartz, muscovite, biotite, almandine-spessartine, apatite |

*This represents a new pegmatite subtype

area and possibly intruded at host rock temperatures as low as 250–300 °C (the brittle-ductile transition in quartzo-feldspathic rocks). However, a few pegmatites of the main set in the Bodengo area actually do show a ductile boundary reactivation developed under high temperature (with an annealed quartz fabric typical of a temperature >500 °C). Hirt *et al*. (2014) measured a magnetic (low-field anisotropy of magnetic susceptibility: AMS) fabric of an aplite dike of the SSB in the lower Maggia valley from where Romer *et al*. (1996) dated post-tectonic aplite-pegmatites at 20.2 + 4.4/–7.8 Ma (zircon U–Pb ages). This dike does not show any discernible foliation or other evidence of internal deformation and crosscuts the mesoscopic foliation of the host gneiss. It does, however, show a magnetic fabric similar to that of the host gneiss, demonstrating that regional deformation was still active in the SSB of the Central Alps at the time of its intrusion and the aplite was in fact deformed. This would imply that the absence of an evident deformation fabric for most of the dikes of the SSB does not necessarily indicate that the dike intrusion totally post-dated the phase of ductile deformation. The absence or rarity of localized ductile deformation of quartz veins (*e.g*., Del Dosso valley) and of miarolitic dikes is more difficult to explain than the case of the aplites. The presence of an earlier set of strongly deformed pegmatites in the Bodengo area indicates that ductile deformation was possible during on-going deformation of the host rock and the absence of deformation must reflect the fading of the deformation event or a post-kinematic emplacement.

*Pegmatite emplacement: a single phase or distinct intrusion events?*

The Codera and Bodengo areas contain pegmatites with a similar mineralogy, which commonly consists, in the non-barren pegmatites, of quartz, feldspar, muscovite, garnet, beryl, and tourmaline (schorl). In contrast, pegmatite dikes from the two areas show marked differences in texture, orientation, and deformation: (1) the pegmatites in the Codera area trend ENE–WSW and are steeply dipping, whereas the main set of the Bodengo area is scattered around a N–S trend and dips steeply to moderately to the east; (2) the former are commonly ductilely deformed, whereas the latter are not (except very locally) and crosscut ductile structures of the SSB; (3) the Bodengo pegmatites are locally miarolitic, whereas the Codera dikes are not. In previous studies, several authors have suggested a relationship between pegmatites and the intrusion of the Novate granite for both the Codera (*e.g*., Wenk 1973) and the Bodengo dikes (Gebauer 1996, Liati *et al*. 2000). In the Bodengo area, this interpretation was based on the fact that the pegmatites crosscut the main ductile fabric, as the Novate intrusion does, and show the same U-Pb zircon ages as the Novate granite (Romer 1996, Gebauer 1996, Liati *et al*. 2000). However, other studies indicate that pegmatite emplacement, at least in the western part of the pegmatite field, was associated with a protracted magmatic activity over a time range from 32 to 20 Ma (Romer *et al*. 1996, Schärer *et al*. 1996, Rubatto *et al*. 2009), with pegmatite emplacement spanning the range from 29 to 25 Ma. It should, however, be noted that the "coincidence" between the age of the pegmatites and of the Novate intrusion is based on just two pegmatites: (1) a pegmatite from Malesco (from the Monte Rosa nappe on the western end of the pegmatite field), discordant to the main SSB foliation (Romer *et al*. 1996), where two distinct xenotime populations yielded U-Pb ages of 25.5 ± 0.2 and 26.5 ± 0.2 Ma; and (2) a discordant pegmatite from San Vittone, located more to the east and within the western side of the Bodengo area (Gebauer 1996). Romer *et al*. (1996) concluded that, in the western part of the pegmatite field, aplites and pegmatites belong to two distinct generations of dikes with overlapping ages and different $^{87}Sr/^{86}Sr$ signatures: (1) ductilely deformed dikes often containing variable amounts of garnet and muscovite with an age range from 32 to 29 Ma and high $^{87}Sr/^{86}Sr$ (0.716–0.735), and (2) discordant, postkinematic pegmatites with an age range from 31 to 26 Ma (and possibly to 20 Ma) and lower $^{87}Sr/^{86}Sr$ (<0.708). The difference in $^{87}Sr/^{86}Sr$ was suggested to indicate different sources and processes involved in the generation of these magmas. Aplites and pegmatites emplaced during Alpine deformation and metamorphism were interpreted to represent mainly melts from the upper crust, whereas post-kinematic and post-metamorphic Alpine dikes involved a larger component from a less evolved source.

Our new data from the Codera and Bodengo pegmatites suggest that, independently of the exact time of dike intrusion (which deserves new dating), pegmatites show a similar degree of evolution and mineral contents. There is, however, a significant difference in the chemistry of some minerals (especially in the garnet composition) between the dikes of the Codera and the Bodengo areas. A possible scenario that could fit with the available data is that the Codera pegmatites are older than the main set of pegmatites in the Bodengo area and possibly also slightly older than the Novate intrusion. This would agree with the observation that pegmatites predate the microgranite dikes crosscutting the Bergell contact, and are related to the Novate intrusion (Wenk 1973). An age of 26.3 ± 1 Ma was obtained by Rb-Sr muscovite dating of a pegmatite from within the Gruf complex in the Piana valley (tributary of the Codera valley) (Hansmann 1996). If this age is interpreted in terms of a muscovite cooling age (*ca*. 500 °C) this also suggests that deformation of the Codera pegmatites actually predated the Novate intrusion, as the Piana valley is about 1 km lower in altitude than the study area in the upper Codera valley. Considering the progressive regional younging of radiometric ages from east to west, which implies a younger cooling of rocks towards the west, and the general discordant character

of the main set of pegmatites with regard to the foliation of the SSB, we infer that pegmatites from the Bodengo area are probably younger than those from the Codera area and could be coeval with the Novate intrusion or younger. In the Bodengo area, the family of pegmatites equivalent to the Codera ones could be represented by the ductilely deformed dikes predating the main set. This scenario remains speculative and new radiometric ages are necessary, together with an estimate of the intrusion conditions of the pegmatite dikes, to validate the interpretation. Pegmatites have a great potential as a marker for precisely dating deformation in the Central Alps and dating of monazite from dikes from both the Bodengo and Codera areas is in progress with this aim.

## Conclusions

The southern part of the Alpine stack of metamorphic units of the Central Alps, which is characterized by a steeply dipping regional foliation (Southern Steep Belt) immediately north of the Periadriatic Fault, hosts the largest (*ca*. 100 × 15 km in areal extent) field of Oligocene (to possibly Miocene) pegmatites. We have investigated these pegmatites in two areas: (1) the Codera area, at the western border of the Bergell batholith (32–28 Ma); and (2) the Bodengo area, more to the east and to the south, between the Mera and Mesolcina valleys (Fig. 1). Field observations indicate the presence of two distinct sets of pegmatites.

The dominant set of pegmatites in the Codera area crosscuts the contact between the Bergell intrusive rocks and the underlying high-grade metamorphic rocks of the Gruf complex. These pegmatites are steeply dipping with a strike around 70° and commonly show a ductile deformation. The deformation temperature has been estimated at ~500 °C. These deformed dikes are crosscut by dikes of Novate-type microgranite.

The dominant set of pegmatites in the Bodengo area crosscuts the regional foliation and are undeformed except for the presence of a local weak ductile overprint. These pegmatites are steeply to moderately dipping towards the W–WNW and comprise dikes with miarolitic cavities.

The two sets of pegmatite have a similar mineral assemblage. Both sets include, together with dominant barren (K-feldspar, quartz, muscovite ± biotite) dikes, differentiated pegmatites containing garnet (almandine-spessartine), beryl, and tourmaline (schorl) as the main minerals. Pegmatites from both areas can be classified in the LCT and mixed LCT-NYF families (with just a single case of NYF pegmatite from the Bodengo area), as indicated by both the presence of Nb-Y oxide and Y-phosphate minerals, and by trace-element geochemistry. The chemical composition of garnet shows a significant difference between the pegmatites of the Codera and the Bodengo areas. All these data together strongly suggest the presence of two distinct generations of dikes within the pegmatite field of the Central Alps.

## Acknowledgements

GP was funded by the Progetto di Ateneo of the Padua University CPDA110128/11 (Exhumed granitoids: A proxy of the deformation at depth in the continental crust). Neil Mancktelow and Jan Cempírek are kindly acknowledged for their reviews. Lee Groat and Pietro Vignola are acknowledged for editorial management. The photographs of the minerals were taken by Roberto Appiani, Stefano Castelli, and Matteo Chinellato. Raul Carampin is thanked for assistance during microprobe analysis.

## References

Balconi, M. (1941) Ricerche petrografiche sulla regione del Serizzo. *Periodico di Mineralogia* **12**, 175–287.

von Blanckenburg, F., Früh-Green, G., Diethelm, K., & Stille, P. (1992) Nd-,Sr-O-isotopic and chemical evidence for a two-stage contamination history of mantle magma in the Central-Alpine Bergell intrusion. *Contributions to Mineralogy and Petrology* **110**, 33–45.

Berger, A., Rosenberg, C., & Schmid, S. (1996) Ascent, emplacement and exhumation of the Bergell pluton within the Southern Steep Belt of the Central Alps. *Schweizerische Mineralogische und Petrographische Mitteilungen* **76**, 357–382.

Brüggmann, H.O. (1965) *Geologie und Pétrographie des südlichen Misox*. Juris-Verlag, Zürich, Switzerland.

Burri, T., Berger, A., & Engi, M. (2005) Tertiary migmatites in the Central Alps: Regional distribution, field relations, conditions of formation, and tectonic implications. *Schweizerische Mineralogische und Petrographische Mitteilungen* **85**, 215–232.

Černý, P. (1982) Petrogenesis of granitic pegmatites *In* Granitic Pegmatites, Science and Industry (P. Černý, ed.). *Mineralogical Association of Canada, Short Course* **8**, 405–461.

Černý, P. (1991a) Rare-element granitic pegmatites, Part I: Anatomy and Internal Evolution of Pegmatite Deposits. *Geoscience Canada* **18**, 29–47.

Černý, P. (1991b) Rare-element granitic pegmatites, Part II: Regional to global environments and petrogenesis. *Geoscience Canada* **18**, 68–81.

Černý, P. & Ercit, T.S. (2005) The classification of granitic pegmatites revisited. *Canadian Mineralogist* **43**, 2005–2026.

Ciancaleoni, L. & Marquer, D. (2006) Syn-extension leucogranite deformation during convergence in the Eastern Central Alps: example of the Novate intrusion. *Terra Nova* **18**, 170–180.

DAVIDSON, C., ROSENBERG, C., & SCHMID, S.M. (1996) Synmagmatic folding of the base of the Berghel pluton, Central Alps. *Tectonophysics* **265**, 213–238.

DE MICHELE, V. (1970) Itinerari Mineralogici della Lombardia. *Natura* **61**, 120, Milano.

DIXON, A., CEMPÍREK, J., & GROAT, L.A. (2014) Mineralogy and geochemistry of pegmatites on Mount Begbie, British Columbia. *Canadian Mineralogist* **52**, 129-164.

DROOP, G.T.R. (1987) A general equation for estimating $Fe^{3+}$ concentrations in ferromagnesian silicates and oxides from microprobe analyses, using stoichiometric criteria. *Mineralogical Magazine* **51**, 431–435.

ERCIT, T.S., ČERNÝ, P., & HAWTHORNE, F.C. (1992) The wodginite group III. Classification and new species. *Canadian Mineralogist* **30**, 633–638.

ERTL, A., HUGHES, J.M., PROWATKE, S., ROSSMAN, G.R., LONDON, D., & FRITZ, E.A. (2003) Mn-rich tourmaline from Austria: structure, chemistry, optical spectra, and relations to synthetic solid solutions. *American Mineralogist* **88**, 1369–1376.

GALLI, A., LE BAYON, B., SCHMIDT, M.W., BURG, J.P., REUSSER, E., SERGEEV, S.A, & LARIONOV, A. (2012) U-Pb zircon dating of the Gruf Complex: disclosing the late Variscan granulitic lower crust of Europe stranded in the Central Alps. *Contributions to Mineralogy and Petrology* **163**, 353–378.

GALLI, A., LE BAYON, B., SCHMIDT, M.W., BURG, J.P., & REUSSER, E. (2013) Tectonometamorphic history of the Gruf complex (Central Alps): exhumation of a granulite–migmatite complex with the Bergell Pluton. *Swiss Journal of Geosciences* **106**, 33–6.

GEBAUER, D. (1996) A P-T-t path (ultra ?) high-pressure ultramafic/mafic rock associations and their felsic country-rock based on SHRIMP dating of magmatic and metamorphic zircon domains. Example: Central Swiss Alps. *In* Earth Processes: Reading the Isotopic Code (A. Basu & S. Hart, eds.). *American Geophysical Union, Monographs* **65**, 307–329.

GRAMACCIOLI, C.M. (1958) Nuovo ritrovamento di delorenzite a Craveggia. *Natura* **49**, 110–112.

GUASTONI, A. (2012) *LCT (lithium, cesium, tantalum) and NYF (niobium, yttrium, fluorine) pegmatites in the Central Alps. Exhumation history, mineralogy and geochemistry*. Ph.D. Thesis, XIV° cycle, Department of Geoscience, University of Padova.

GUASTONI, A. & GRAMMATICA, P. (2001) Silicati di berillio della valle Soe. *Rivista Mineralogica Italiana* **25**, 105–107.

GUASTONI, A. & DEMARTIN, F. (2003) Ferrotapiolite della valle Soè. *Atti della Società Italiana di Scienze Naturali* **144**, 145–150.

GUASTONI, A., DEMARTIN, F., & PEZZOTTA, F. (2004) U-rich microlite from granitic pegmatites of Codera valley in the Masino-Bregaglia Massif (Sondrio province). *Atti della Società Italiana di Scienze Naturali* **145**, 359–365.

GUASTONI, A., NESTOLA, F., MAZZOLENI, G., & VIGNOLA, P. (2007) Mn-rich graftonite, ferrisicklerite, staněkite and Mn-rich vivianite in a granitic pegmatite at Soè Valley, central Alps, Italy. *Mineralogical Magazine* **71**, 579–585.

HÄNNY, R., GRAUERT, B., & SOPTRAJANOVA, G. (1975) Paleozoic migmatites affected by high-grade Tertiary metamorphism in the Central Alps (Valle Bodengo, Italy). *Contributions to Mineralogy and Petrology* **51**, 173–196.

HANSMANN, W. (1996) Age determination on the Tertiary Masino-Bregaglia (Bergell) intrusives (Italy, Switzerland): a review. *Schweizerische Mineralogische und Petrographische Mitteilungen* **76**, 421–451.

HIRT, A.M., BIEDERMANN, A.R., & MANCKTELOW, N.S. (2014) Magnetic study of a late Alpine dike crosscutting the regional foliation. *Tectonophysics* (in press).

HÜBER. R.K. (1993) *Ein Beitrag zur Geologie des südlichen Misox*. Unpublished diploma thesis. ETH-Zürich. Switzerland.

JÄGER, E. (1962) Rb-Sr age determinations on micas and total rocks from the Alps. *Journal of Geophysical Research* **67**, 5293–5306.

JENNY, H., FRISCHKNECHT, G., & KOPP. J. (1923) Geologie der Adula. *Beiträge zur Geologischen Karte der Schweiz* N.F. **51**.

KÖPPEL, V., GÜNTHERT, A., & GRÜNENFELDER, M. (1980) Patterns of U-Pb zircon and monazite ages in polymetamorphic units of the Swiss Central Alps. *Schweizerische Mineralogische und Petrographische Mitteilungen* **61**, 97–119.

LEISS, B. (2005) New techniques, measuring strategies and applications of conventional X-ray texture analysis. *Deformation Mechanism, Rheology and Tectonics, Conference Abstracts*, Zurich, Switzerland (130).

LEISS, B. & ULLEMEYER, K. (2006) Neue Perspektiven der Texturanalytik von Gesteinen mit konventioneller Röntgenbeugung. *In* Symposium "Tektonik, Struktur und Kristallingeologie" (S. Phillipp, B. Leiss, & A. Vollbrecht eds.). Universitätsverlag Göttingen, Germany (128–130).

LIATI, A., GEBAUER, D., & FANNING, M. (2000) U-Pb SHRIMP dating of zircon from the Novate granite (Bergell, Central Alps): evidence for Oligocene-Miocene magmatism, Jurassic/Cretaceous continental rifting and opening of the Valais trough. *Schweizerische Mineralogische und Petrographische Mitteilungen* **80**, 305–316.

LONDON, D. (1992) The application of experimental petrology to the genesis and evolution of granitic pegmatites. *Canadian Mineralogist* **30**, 499–540.

London, D. (2008) Pegmatites. *Mineralogical Association of Canada Special Publication* **10**, 347.

Mancktelow, N.S. & Pennacchioni, G. (2005) The control of precursor brittle fracture and fluid-rock interaction on the development of single and paired ductile shear zones. *Journal of Structural Geology* **27**, 645–661.

Mancktelow, N.S. & Pennacchioni, G. (2013) Late magmatic healed fractures in granitoids and their influence on subsequent solid-state deformation. *Journal of Structural Geology* **57**, 81–96.

Matthies, S. & Vinel, G.W. (1982) An example demonstrating a new reproduction method of the ODF of texturized samples from pole figures. *Physica Status Solidi B* **112**, K115–K120; doi:10.1002/pssb. 2221120255.

Milnes, A.G. (1974) Structure of the Pennine Zone (Central Alps): a new working hypothesis. *Geological Society of America Bulletin* **85**, 1727–1732.

Nagel, T., De Capitani, C., Frey, M., Froitzheim, N., Stunitz, H., & Schmid, S.M. (2002) Structural and metamorphic evolution during rapid exhumation in the Lepontine dome (southern Simano and Adula nappes, Central Alps, Switzerland). *Eclogae geologicae Helvetiae* **95**, 301–321.

Oberli, F., Meier, M., Berger, A., Rosenberg, C., & Gieré, R. (2004) U-Th-Pb and $^{230}Th/^{238}U$ disequilibrium isotope systematics: Precise accessory mineral chronology and melt evolution tracing in the Alpine Bergell intrusion. *Geochimica et Cosmochimica Acta* **68**, 2543–2560.

Peco, G. (1949) Le pegmatite a berillo di Val Codera (Sondrio). *L'industria della ceramica e dei silicati* **10**, 7–9.

Pennacchioni, G. (2005) Control of the geometry of precursor brittle structures on the type of ductile shear zone in the Adamello tonalites, Southern Alps (Italy). *Journal of Structural Geology* **27**, 627–644.

Pennacchioni, G. & Mancktelow, N.S. (2007) Nucleation and initial growth of a shear zone network within compositionally and structurally heterogeneous granitoids under amphibolite facies conditions. *Journal of Structural Geology* **29**, 1757–1780.

Pennacchioni, G. & Zucchi, E. (2013) High-temperature fracturing and ductile deformation during cooling of a pluton: the Lake Edison granodiorite (Sierra Nevada batholith, California). *Journal of Structural Geology* **50**, 54–81.

Pennacchioni, G., Menegon, L., Leiss, B., Nestola, F., & Bromiley, G. (2010) Development of crystallographic preferred orientation and microstructure during plastic deformation of natural coarse-grained quartz veins. *Journal of Geophysical Research* **115(B12)**, 405, doi:10.1029/2010JB007674.

Pouchou, J.L. & Pichoir, F. (1985) "PAP" (phi-rho-z) procedure for improved quantitative microanalysis. *In* Microbeam Analysis (J.T. Amstrong, ed.). San Francisco Press, San Francisco, California, United States (104–106).

Reusser, C.E. (1987) Phasenbeziehungen im Tonalit der Bergeller Intrusion. *Ph.D. thesis*, ETH Zürich.

Roggiani, A.G. (1966) Il filone di feldspato sodico dell'Alpe Rosso a monte di Orcesco (valle Vigezzo). *Illustrazione Ossolana* **8(1)**, 23–45.

Romer, R.L., Schärer, U., & Steck, A. (1996) Alpine and pre-Alpine magmaism in the root-zone of the western Central Alps. *Contributions to Mineralogy and Petrology* **123**, 138–158.

Rosenberg, C. (2004) Shear zones and magma ascent: A model based on a review of the Tertiary magmatism in the Alps. *Tectonics* **23**, TC3002.

Rubatto, D., Hermann, J., Berger, A., & Engi, M. (2009) Protracted fluid-induced melting during Barrovian metamorphism in the Central Alps. *Contribution to Mineralogy and Petrology* **158**, 703–722.

Schärer, U., Cosca, M., Steck, A., & Hunziker, J. (1996) Termination of major ductile strike-slip shear and differential cooling along the Insubric line (Central Alps): U-Pb, Rb-Sr and 40Ar/39Ar ages of cross-cutting pegmatites. *Earth and Planetary Science Letters* **142**, 331–351.

Spezia, G. (1882) Sul berillo di Craveggia. *Atti della Regia Accademia delle Scienze di Torino* **17**, 769.

Stern, W.B. (1966) Zur Mineralchemie von Glimmern aus Tessiner Pegmatiten. *Schweizerische mineralogische und petrographische Mitteilungen* **86**, 137–188.

Stipp, M., Stünitz, H., Heilbronner, R., & Schmid, S.M. (2002) The eastern Tonale fault zone: A 'natural laboratory' for crystal plastic deformation of quartz over a temperature range from 250 to 700 °C. *Journal of Structural Geology* **24**, 1861–1884.

Strüver, G. (1885) Sulla columbite di Craveggia in Val Vigezzo. *Rendiconti Regia Accademia dei Lincei* **1**, 8–9.

Studer, B. (1851) *Geologie der Schweiz*. Stämpfli, Bern, Germany (485).

Taddei, C. (1940) Pegmatiti della Svizzera Italiana e minerali in esse contenuti. *Schweizerische Mineralogische und Petrographische Mitteilungen* **20**, 247–252.

Vignola, P., Gatta, G.D., Hatert, F., Guastoni, A., & Bersani, D. (2014) On the crystal-chemistry of a near end-member triplite, $Mn_2^{2+}(PO_4)F$, from Codera valley (Sondrio Province, Central Alps, Italy). *Canadian Mineralogist* **52**, 235-245.

Villa, I.M. (1998) Isotopic closure. *Terra Nova* **10**, 42–47.

Wassermann, G. & Grewen, J. (1962) *Texturen metallischer Werkstoffe*. Springer-Verlag, Berlin, Germany.

WEBBER, K.L., FALSTER, A.U., SIMMONS, W.B., & FOORD, E.E. (1997) The Role of diffusion-controlled oscillatory nucleation in the formation of line rock in pegmatite–aplite dikes. *Journal of Petrology* **38(12)**, 1777–1791.

WENGER, M. & ARMBRUSTER, T. (1991) Columbite (Fe,Mn)$(Nb,Ta)_2O_6$ in the pegmatites of the calc-alkaline Bergell intrusion (southeast Central Alps). *Schweizerische Mineralogische und Petrographische Mitteilungen* **71**, 349–369.

WENGER, M., KRÄHENBÜHL, U., & ARMBRUSTER, T. (1993) REE characteristics in pegmatites and adjacent wall rocks of the calc-alkaline Bergell intrusion (southeastern Central Alps). *Schweizerische Mineralogische und Petrographische Mitteilungen* **73**, 383–389.

WENK, E. (1970) Zur Regionalmetamorphose und Ultrametamorphose im Lepontin. *Fortschritte der Mineralogie* **47**, 34–51.

WENK, H.R. (1973) The structure of Bergell Alps. *Eclogae geologicae Helvetiae* **66**, 255–291.

WENK, H.R. (1985) *Preferred orientation in deformed metals and rocks: An introduction to modern texture analysis*. Academic Press, Orlando, Florida, United States.

WENK, H.R., MATTHIES, S., DONOVAN, J., & CHATEIGNER, D. (1998) BEARTEX: a Windows-based program system for quantitative texture analysis. *Journal of Applied Crystallography* **31**, 262-269.

ZAMBONINI, F. (1907) Strüverite, un nuovo minerale. *Rendiconto dell'Accademia delle Scienze Fisiche e Matematiche, Sezione della Società Reale di Napoli* **13**, 35–41.

ZAMBONINI, F. (1908) Delorenzite, un nuovo minerale**.** *Rendiconto dell'Accademia delle Scienze Fisiche e Matematiche, Sezione della Società Reale di Napoli* **13*, 35–51*.**

ZHANG, C., GIERE, R., STÜNITZ, H., BRACK, P., & ULMER, P. (2001) Garnet-quartz intergrowths in granitic pegmatites from Bergell and Adamello, Italy). *Schweizerische Mineralogische und Petrographische Mitteilungen* **81**, 89–113.

ZWINGMANN, H. & MANCKTELOW, N. (2004) Timing of Alpine fault gouges. *Earth and Planetary Science Letters* **223**, 415–425.

*Received February 28, 2014. Revised manuscript accepted April 14, 2014.*

## APPENDIX: ANALYTICAL METHODS

*X-ray texture goniometry*

The Crystallographic Preferred Orientation (CPO) of quartz was determined for quartz mylonites by X-ray texture goniometry (TG). The pole figure measurements for quantitative texture analysis were carried out using a PANalytical X-ray texture measuring system installed at the Geoscience Centre of the University of Göttingen, Germany (Leiss 2005, Leiss & Ullemeyer 2006). A poly-capillary glass fiber lens at the primary beam side provides high X-ray intensities, an optically parallel beam, and an exceptionally large beam size of up to 7 mm. This allows a short measuring time per pole figure (1s per pole figure direction at an anode current of 40 mA and a voltage of 40 kV), a high resolution, and a relatively large measured volume. Computer-controlled sample movement allows automated measurements of a series of local textures on a regular or irregular grid within a polished sample area of 100 × 100 mm. This provides a control on the texture homogeneity of the sample texture and/or improves the measuring statistics, especially for coarse-grained samples, by accumulating several pole-figure measurements into a bulk pole figure. A standard pole-figure measuring grid of 5° × 5° was applied for quartz (100), (101), (110)(<*a*> axis), (102), (111), (200), (201), (112), (211), and for background measurement. After subtraction of the background from the quartz measurements, a defocusing correction based on functions derived from pole figure measurements of quartz powder (*e.g.*, Wassermann & Grewen 1962, Wenk 1985) was carried out. At high tilt angles, reasonable defocusing corrections are not possible, therefore measurements were cut off at a tilt angle of 85°, leading to incomplete pole-figures. The orientation distribution function (ODF) values in three-dimensional orientation space were calculated by means of the WIMV algorithm (Matthies & Vinel 1982), included in the BEARTEX software package (Wenk *et al*. 1998). From the results of the ODF, full pole-figures and pole-figures that cannot be directly measured, such as quartz (001)(*c* axis), were calculated.

*Electron Microprobe analysis*

Chemical compositions of selected mineral phases were obtained using a CAMECA SX-50 electron microprobe equipped with four wavelength dispersive spectrometers and one energy dispersive spectrometer at the laboratory of microanalysis of the Institute for Geosciences and Earth Resources of CNR (Padua). The operating conditions were 20 kV accelerating voltage and 20 nA beam current. Counting times were 10 s at the peak and 5 s at the background for major elements and 20 to 100 s at peak and background for minor elements. Details on the analytical conditions are reported in Guastoni (2012). X-ray counts were converted into oxide weight percentages using the PAP correction program (Pouchou & Pichoir 1991). Analyses are precise to within 1% for major elements and 3–5% for minor elements. Calibration was carried using natural and synthetic international standards in part supplied by Cameca and in part kindly provided by the Smithsonian National Museum of Natural History (Smithsonian Microbeam Standards).

*ICP-OES and ICP-MS analyses*

Bulk rock and trace element analysis were performed by Inductively Coupled Plasma-Optical Emission Spectrometry (ICP-OES) and Inductively Coupled Plasma-Mass Spectrometry (ICP-MS) at Acme Analytical Laboratories Ltd. (Vancouver, Canada), accredited under ISO 9002. For analysis, the sample powders (10 g each) were mixed with lithium metaborate/tetraborate and fused to glass beads (at 1100 °C) in a furnace. The beads were then dissolved in nitric acid. The major elements (Si, Al, Fe, Mg, Ca, Na, K, Ti, and P) and Ba were analyzed by inductively coupled plasma optical emission spectrometry using a Spectro Ciros instrument. Loss on ignition ($H_2O$ and $CO_2$) was determined by weight difference after ignition at 1000 °C. Sulfur was analyzed by combustion, using a LECO CS-200 analyzer. Trace elements were analyzed by ICM-MS using a Perkin-Elmer instrument, after lithium metaborate fusion and dilute nitric acid digestion (Cs, Hf, Nb, Rb, Sr, Nb, Ta, Th, U, V, Hf, Zr, Y, and REE) or after Aqua Regia digestion at 95 °C for 1 h for heavy metals and metalloids (Mo, Cu, Pb, Zn, Ni, As, Cd, Sb, Bi, Ag, Au, Hg, Tl, Se, Co, Cr, Pd, and Pt). The accuracy and precision of the trace element data were about 5%.